

Article

Analysis of Thermally Induced Strain Effects on a Jointed Rock Mass through Microseismic Monitoring at the Acuto Field Laboratory (Italy)

Guglielmo Grechi ^{1,*}, Danilo D'Angiò ² and Salvatore Martino ¹

¹ Earth Sciences Department of Sapienza University of Rome and Research Center for Geological Risks (CERI), 00185 Rome, Italy

² Department for the Geological Survey of Italy at the Italian Institute for Environmental Protection and Research (ISPRA), 00144 Rome, Italy

* Correspondence: guglielmo.grechi@uniroma1.it

Abstract: The study of the deformation of rock masses in response to near-surface thermal stresses is nowadays considered crucial in the field of geological risk mitigation. The superposition of heating and cooling cycles can influence the mechanical behavior of rock masses by inducing inelastic deformations that can trigger shallow slope instabilities, such as rockfalls and rock topples. This study reports the main outcomes obtained from the analysis of 20 month long microseismic monitoring at the Acuto field laboratory (Central Italy), where an integrated geotechnical and geophysical monitoring system has been operating since 2015. A preliminary event classification was performed through the analysis of time- and frequency-domain characteristic features of the extracted waveforms. Furthermore, the evolution of the local microseismicity was explored as a function of environmental factors (i.e., rock and air temperature, thermal gradients and ranges, and rainfalls) to highlight potential correlations. The here presented results highlight nontrivial insights into the role played by continuous near-surface temperature fluctuations and extreme thermal transients in influencing the stability of rock masses. In particular, the comparison of monitoring periods characterized by the most intense microseismic activity highlights a peculiar distribution of microseismicity during the heating and cooling phases of the rock mass in relation to different environmental conditions. These behaviors can be interpreted as the consequence of different driving mechanisms at the base of local failures.

Keywords: rock mass; microseismic monitoring; temperature fluctuations; field laboratory



Citation: Grechi, G.; D'Angiò, D.; Martino, S. Analysis of Thermally Induced Strain Effects on a Jointed Rock Mass through Microseismic Monitoring at the Acuto Field Laboratory (Italy). *Appl. Sci.* **2023**, *13*, 2489. <https://doi.org/10.3390/app13042489>

Academic Editor: Roberto Tomás

Received: 16 January 2023

Revised: 11 February 2023

Accepted: 14 February 2023

Published: 15 February 2023



Copyright: © 2023 by the authors. Licensee MDPI, Basel, Switzerland. This article is an open access article distributed under the terms and conditions of the Creative Commons Attribution (CC BY) license (<https://creativecommons.org/licenses/by/4.0/>).

1. Introduction

The last decades have seen a significantly increasing scientific interest in studying the thermomechanical effects on jointed rock masses caused by near-surface temperature fluctuations. The in situ monitoring and quantification of thermally induced damaging processes on jointed rock masses constitutes a frontier nowadays in the field of landslide risk mitigation of natural and anthropized rock slopes. The analysis of thermomechanical effects on jointed rock masses has been widely approached through comparative analyses (statistical and observational-based approaches) of temperature and stress–strain long-term monitoring timeseries. Several studies established a strong correlation between near-surface temperature fluctuations and rock mass deformations [1–7], demonstrating the existence of inelastic trends even in the absence of transient and violent phenomena such as heavy rainfalls, strong winds, or local seismicity, which are frequently considered to be the primary triggering factors of plastic strain. More recently, passive seismic monitoring techniques have been widely exploited to identify and study thermally driven deformations in rock masses. Ambient seismic noise, microseismic activity, and acoustic emission monitoring techniques showed the greatest potential in providing new insights into rock mass

fracturing processes. These techniques proved to be useful in highlighting how daily and annual oscillations of near-surface temperatures can cause evident changes in the stability of jointed rock masses, ultimately impacting the evolution in time of already recognized slope instabilities on various dimensional scales [8–17]. The exploitation of high-sensitivity seismic sensors for studying rock mass instabilities has well-constrained the existence of cause-and-effect relationships between growing instability conditions and microseismic activity [8,15,18]. Furthermore, they have shown great potential in providing precursory patterns of failure events [19,20]. In the framework of structural health monitoring of natural and anthropic structures, microseismic (MS) signal analysis nowadays represents one of the most widespread diagnostic tools in several fields of application [12,17,21–23]. MS events are low-energy seismic signals genetically related to the occurrence of plastic deformations within a medium. It is well known that when internal relative slips or the propagation of fractures occur due to the reaching of a strain threshold, the energy stored in a medium is sharply released in the form of elastic waves, leading to infrasonic, sonic, or MS signals [24]. MS monitoring mainly focuses on analyzing signals characterized by a wide range of frequency contents, spanning from 10^1 to 10^3 Hz, thus ranking between the traditional earthquake and seismological studies and the acoustic emission domain (Figure 1) [25]. Depending on the characteristics of the site under investigation, MS sensors can be arranged in different array configurations (e.g., varying their location, distance, and density) to surround the monitoring target properly [26].

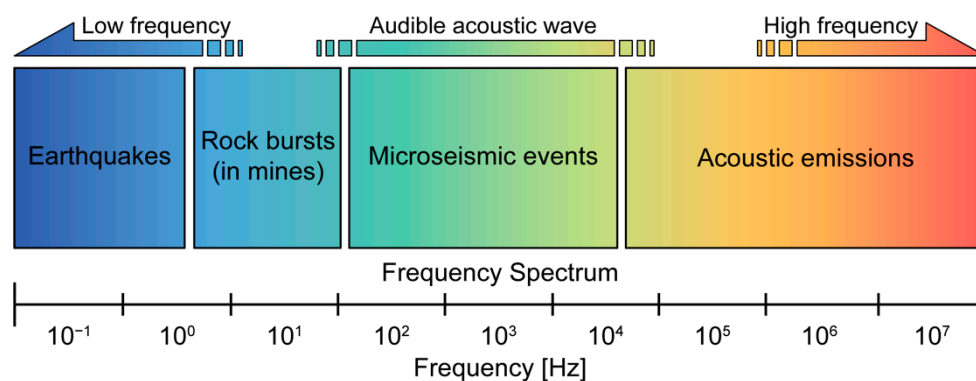


Figure 1. Seismic motion wave frequency spectrum and field of application of MS monitoring.

MS data processing generally starts with the detection and extraction of signals of interest embedded within ambient seismic noise recordings. The recognition of MS waveforms related to fracturing processes can strongly influence the size and accuracy of collected datasets to be analyzed. Numerous techniques exist for recognizing MS events and are based on the analysis of frequency- and time-domain features [27,28]. After MS events are identified, they can be analyzed, classified, and localized to investigate source parameters and failure mechanisms [26]. MS event classification is a critical step in data processing as it guarantees that no suspicious or artificial waveforms are contained in a dataset, also enabling the recognition of different MS event classes [29]. This task is generally accomplished through manual or automatic analyses of several parameters, such as envelope shape, event duration, frequency, and energy content of signals. On this topic, several authors have proposed the semi-automatic and automatic classification of MS events through visual screening and supervised or unsupervised machine learning techniques [21,29–32]. The recent development of high-sensitivity sensors capable of detecting very low amplitude seismic signals paved the way for innovative applications of MS monitoring in civil engineering [33–36], mining and quarrying activities [37–39], tunneling excavation [40], and slope stability [8,13,19,41–44]. Concerning the application of MS monitoring techniques for rock slope stability, several case studies are present in the literature where high-sensitivity seismic networks were deployed to test their performance in deciphering the evolution of slope instabilities (i.e., both in soil and rock) [18,19,43]. When dealing with the study of

microseismicity in jointed rock masses, the analysis and characterization of temporal rates, peak ground acceleration, energy, and frequency content, are among the most employed strategies to study the evolution of rock mass failures. Correlations between microseismicity and environmental factors (e.g., rainfalls, snowfalls, air temperature, and wind) have been studied by several authors since seismic monitoring networks have proven to be valuable tools for the identification of fracturing processes in jointed rock masses. Most of these studies are focused on high-mountainous regions, where thermal regimes are characterized by continuous fluctuations in temperature around freezing conditions [15,19,44].

The continuous action of thermal cycles can be regarded as a “preparatory” factor of progressive failure in rock masses. In this framework, the investigation of rock mass damaging (RMD) requires the implementation of monitoring systems capable of dealing with the timescale of failure mechanisms and the dimensional scale of rock mass instabilities. Therefore, it is good practice to collect multiparametric datasets to consider all possible factors contributing to reversible or irreversible changes in mechanical and dynamic parameters over different timescales.

To better constrain the role of temperature fluctuations in driving reversible and irreversible deformations of jointed rock masses, we present the results obtained from the analysis of a 20 month long MS monitoring dataset collected at the Acuto field laboratory [45]. The test-site is located within an abandoned quarry in Central Italy, and it is managed by the Department of Earth Sciences and the CERI—Research Center for Geological Risks of Sapienza University of Rome. It hosts an integrated geotechnical and geophysical monitoring system installed on a 20 m³ prone-to-fall rock block. The here presented experimental activities were designed to investigate the role of near-surface temperature fluctuations in causing the progressive growth and propagation of cracks in prone-to-fall rock masses. For this purpose, we analyzed the continuous ambient vibrations collected over almost two years of monitoring campaigns. At first, a semi-automatic approach was implemented to identify the most intense events and perform a preliminary classification of the recorded waveforms. This task was also designed to exclude false events from further consideration. Hence, the monitoring dataset was analyzed by comparing the evolution and characteristics of the local microseismicity with environmental factors to shed light on potential correlations that could reveal precursory patterns for rock mass instabilities.

2. Case Study: The Acuto Field Laboratory

The Acuto field laboratory is located in the westernmost sector of an abandoned limestone quarry (Prenestina quarry) within the Municipality of Acuto (Central Italy) (Figure 2). It was designed and instrumented starting from November 2015 in the framework of multiple experimental activities managed by the CERI of Sapienza University of Rome. This natural test-site aims to investigate the ability of an integrated multiparametric monitoring system to decipher the role of environmental and anthropic stresses in determining the worsening of rock mass stability. The abandoned quarry, which is a few hundred meters NE from Acuto, is found on a monoclinic SW-dipping carbonate slope, where a succession of Meso-Cenozoic limestones is affected by NW–SE striking normal faults with offsets up to 10 m [46]. The monitoring system consists of several geotechnical and geophysical devices and was installed on the vertical rock wall outcropping in the western sector of the abandoned quarry. After a preliminary surveying stage and geomechanical characterization, a potentially unstable 20 m³ rock block was identified as the main target of monitoring activities [47]. This element was selected due to its severe fracturing degree and the presence of a rear discontinuity detaching the rock block from the quarry wall behind, thus predisposing this volume toward instability (Figure 2a). The monitoring system consists of (i) one temperature probe for rock mass temperature, (ii) six strain gauges installed in correspondence with microcracks, (iii) four extensometers installed on open fractures, and (iv) two fully equipped weather stations. The system is cable-connected to a Campbell Scientific CR1000 data logger collecting data with a 1 min sampling rate. Apart from the

permanently installed devices on the rock block, the spectrum of monitoring activities at the Acuto field laboratory was enriched by several experimental activities carried out over the years.

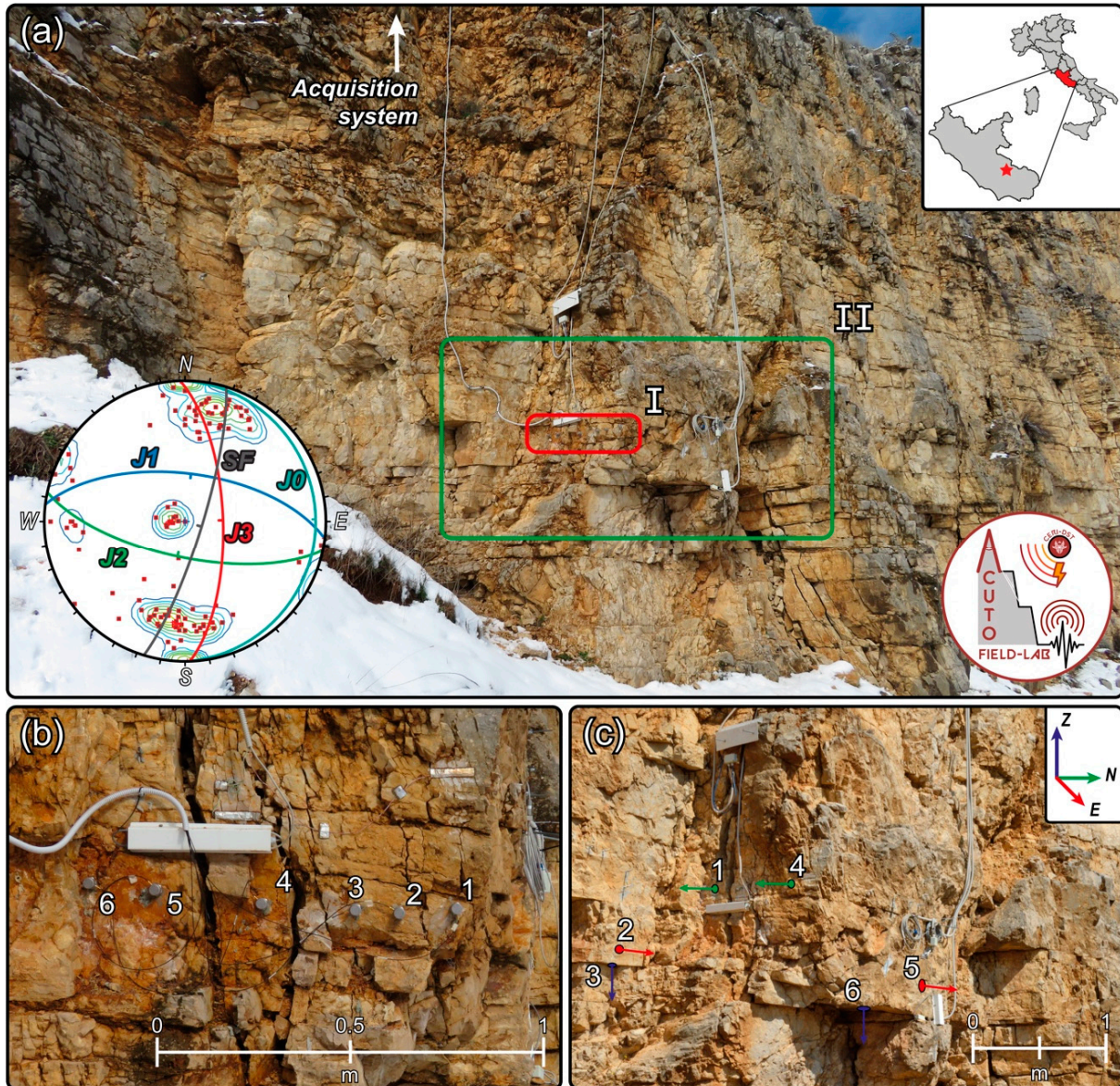


Figure 2. View of the monitored jointed rock block at the Acuto field laboratory (<https://www.dst.uniroma1.it/en/structures/laboratories/NaturalLaboratoryAcuto>) along with the stereographic projection (equal-angle lower hemisphere) of pole density distributions and planes of the four main discontinuity sets (SF: slope face) (a). The two boxes help to better visualize the different volumes involved by the configurations adopted during the first (I, red box) and the second monitoring campaign (II, green box). Between February and May 2018, six micro-accelerometers (1–6) were deployed along a linear alignment specifically designed to mark the transition from the stable rock mass to the unstable rock block (b). The second monitoring campaign (November 2018–October 2019) was conducted by installing six micro-accelerometers (1–6) in a “composite” double three-component configuration (c).

These activities were designed to study the effect of preparatory factors on rock slope instabilities and test novel methodologies for the investigation of progressive damaging processes in jointed rock masses [48–50]. From 2018 to 2019, an MS monitoring array composed of several one-component micro-accelerometers was installed on the rock block and

the contiguous rock wall. This system perfectly integrated with the already existing one, providing interesting insights into the dynamic and deformational response of the studied rock block in response to continuous and transient environmental stresses [18,23,24]. The monitoring array was composed of six one-component piezoelectric micro-accelerometers (Bruel & Kjaer type 8344). All sensors were connected via low-noise cables to an HBM SomatXR MX1601B-R signal amplifier coupled with a SomatXR CX23-R digital data controller, and set to a sampling frequency of 2400 Hz. The piezoelectric micro-accelerometers were selected due to their optimized design for low-frequency and low-level vibration measurements, as witnessed by their high sensitivity (2500 mV/g) and flat frequency response from 5 to 2 kHz. The power supply was constantly guaranteed by means of external backup batteries and one solar panel; however, several gaps exist in the monitoring dataset due to frequent system malfunctions. Two different long-term monitoring campaigns were carried out from February 2018 to November 2019. These campaigns are mainly differentiated because two distinct array configurations were designed and implemented. During the first campaign (February 2018–May 2018), six one-component micro-accelerometers were deployed in a linear array on the back face of the rock block—where the vertical open joint partially detaches the rock block from the rock wall (Figure 2b)—with regular 15 cm spacing. During the second campaign (November 2018–October 2019), a different array configuration was designed, and the micro-accelerometers were deployed in a “composite” three-component setting to investigate potential differences between the dynamic behavior of the rock wall and the rock block (Figure 2c).

3. Methods

The continuous ambient vibrations collected at the Acuto field laboratory were processed following an approach based on the automatic extraction of energetic events and the preliminary classification of waveforms via manual inspection. This step is often considered paramount to constituting a reliable dataset of MS events and thus excluding false events from consideration. The flow chart of Figure 3 describes the adopted workflow. The automatic detection of MS signals embedded within ambient seismic noise recordings was performed using an STA/LTA triggering algorithm. Firstly, seismic recordings were preprocessed by applying automatic demeaning, detrending, and high-pass filtering above 2 Hz to remove any potential disturbances at very low frequencies. The STA/LTA algorithm was then launched on every file containing absolute acceleration values recorded from each channel of the array. This algorithm is one of the most exploited techniques for detecting seismic transients in various seismological contexts [51,52], enabling the identification of energetic signals over ambient noise. The functioning principle of the STA/LTA trigger algorithms relies on the analysis of the ratio between the average amplitude of signals computed over two different moving windows. The STA (short-time average) measures the instant amplitude of the signal, and it is sensitive to transient energetic events, while the LTA (long-time average) quantifies the average amplitude of the background noise. The STA/LTA ratio is continuously computed and when it exceeds a user-defined triggering threshold an event is declared, and the related signal is registered until the ratio decreases to a detragging level. Even though STA/LTA algorithms are among the most widely exploited techniques for the detection of seismic events, the calibration of the triggering threshold and the length of the moving windows represent major challenges. This calibration step should always be performed by considering the characteristics of the events and the characteristic background noise at the site under investigation [28]. In general, STA windows 2–3 times greater than the dominant period of the MS signal and LTA windows 10–100 times greater than the STA window size generally produce good quality results. This calibration step was performed through the preliminary analysis of training datasets aimed at defining the best tuning of STA/LTA parameters. For the scope of this study, the size of STA and LTA windows was set to 0.1 s and 10 s, with triggering and detragging thresholds fixed to 4.

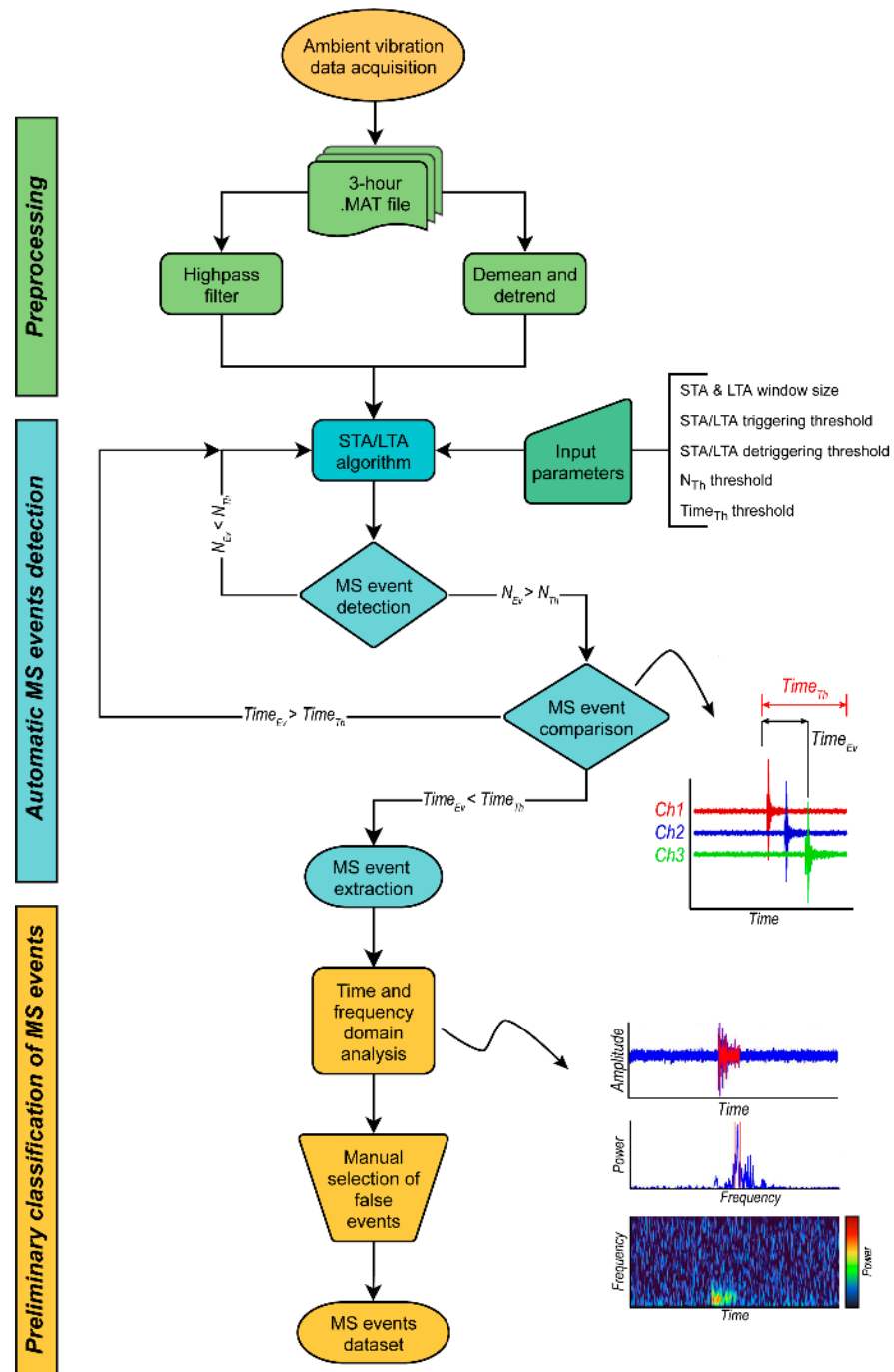


Figure 3. Flow chart summarizing the adopted workflow for the automatic detection and preliminary classification of MS events from ambient seismic noise continuous recordings.

Pre- and post-event time windows were also set to 5 s to avoid possible losses in information on coda waves or multiple events. Instead of running the event detection algorithm singularly on every channel, the adopted procedure was designed to simultaneously compare all channels of the monitoring array to better identify synchronous events. To this aim, and to avoid the collection of false events triggered by electrical and spurious transients, this procedure embedded two conditions that had to be mandatorily satisfied to declare an MS event. The first condition was related to the number of channels triggered by the same MS event: when the number of triggered channels (N_{Ev}) was equal to or greater than a user-defined threshold (N_{Th}), the event was extracted. The second condition required that the time interval between the arrival time on the first and last triggered channels (T_{Ev})

must be shorter than a user-defined duration (T_{Th}) that starts in correspondence with the first arrival of the MS event. When both conditions were satisfied, the event was extracted and further analyzed. In this study, the minimum number of triggered channels (N_{Th}) to declare an event was set to 4, while the maximum time interval (T_{Th}) was set to 0.15 s. It is worth specifying that the first condition (N_{Th}) was found to be the most dominant in constraining the number of MS events detected by the STA/LTA algorithm. This threshold can vary from one up to the maximum number of channels, and the higher its level, the greater the coherence of signals and the reliability of MS events. In contrast, when dealing with low signal-to-noise ratio recordings, it is not rare to miss the detection of events due to different factors that can significantly affect monitoring arrays (e.g., the distance between sensors, the presence of fractures or potential malfunctioning) and a highly conservative threshold can lead to a potential loss in information. Using the aforementioned STA/LTA parameters, it was possible to build an MS dataset of 864 events.

After the automatic event identification and extraction, a preliminary classification of the collected signals was performed to discriminate between MS and false events. This stage of the analysis always represents a major task in MS monitoring, and it becomes crucial when potential correlations between environmental factors and microseismicity must be investigated. To this aim, a preliminary classification of signals was performed through the manual inspections of waveforms, power spectra, and spectrograms of every detected event. Such an analysis allowed us to concurrently investigate the coherency of time- and frequency-domain characteristics of signals over all of the channels of the array, leading to a significant reduction in the number of events (Figure 4).

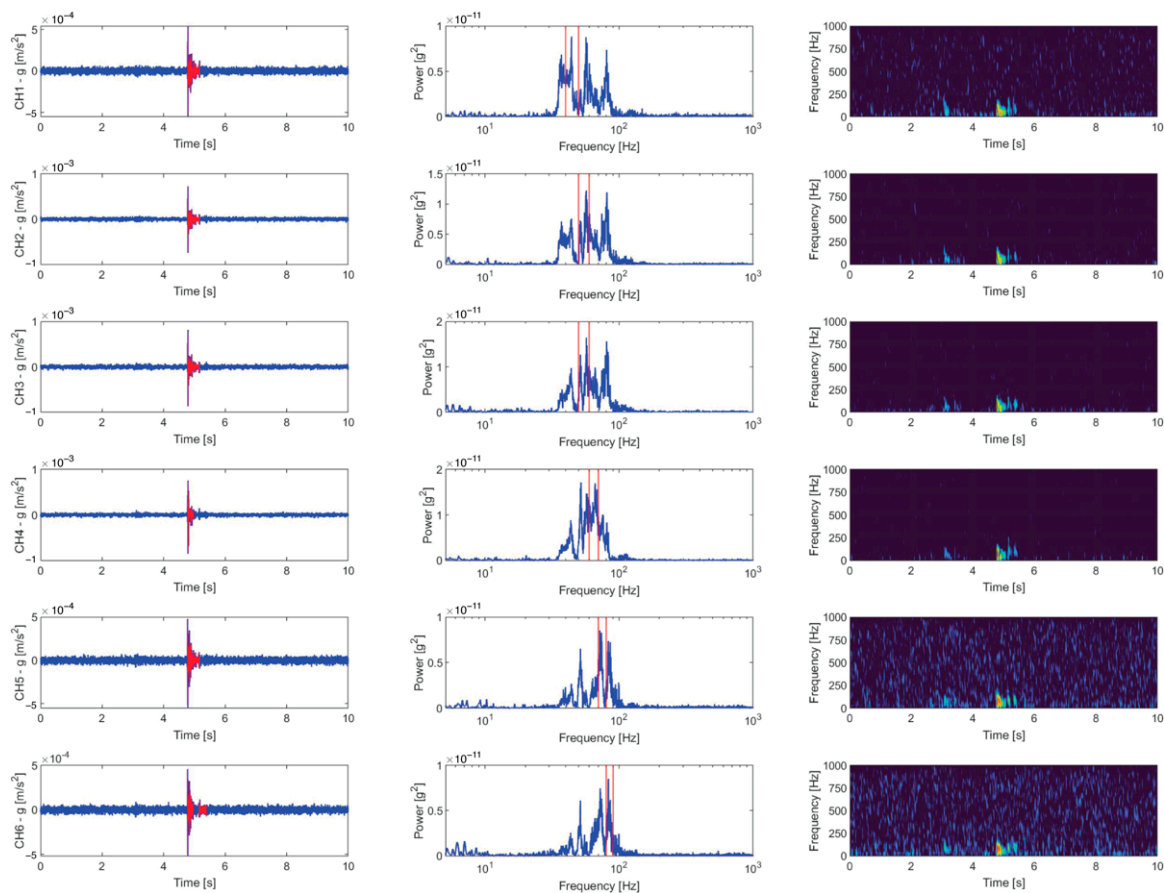


Figure 4. Example of one event automatically detected and classified as an MS event through visual screening of its time- and frequency-domain features (left: signal waveform; center: power spectral density estimate; right: spectrogram).

To strengthen the results of the manual classification and to reduce the influence of subjectivity on the analysis, a statistical comparison between time- and frequency-domain characteristics of MS and false events was performed. This task is generally conducted by implementing fully or semi-automatic procedures that rely on machine learning algorithms—such as hidden Markov models (HMMs) [53], support vector machines (SVMs) [54], linear discriminant analysis (LDA) [8], fuzzy logic (FL) [55], random forest (RF) [56], convolutional neural networks (CNNs) [57], and k-means clustering [21]—to identify recurrent classes of events. For this study, a preliminary attempt was made to strengthen the affordability of the manual screening procedure. The whole dataset was investigated by analyzing multiple time- and frequency-domain parameters of the manually classified events following the workflow proposed by Colombero [21].

In the time domain, signals were analyzed by extracting information on their duration, shape, and energy content. Concerning their shape, three parameters were considered: the maximum amplitude (A_{\max} or PGA—peak ground acceleration), the normalized amplitude (A_{\max}/A_{mean}), and the kurtosis of the signal envelope. Concerning their duration, bracketed and uniform durations were computed. The bracketed duration was retrieved as the time interval comprised between the first and the last exceedance of the signal over a fixed threshold. In contrast, the uniform duration is defined as the sum of all time intervals in which the signal exceeds the same threshold [58].

The Arias intensity (I_A) was also calculated to evaluate the energy content associated with every event. This parameter is a measure of the cumulative intensity of ground motion obtained as the integral of the squared acceleration of the seismic signal:

$$I_A = \frac{\pi}{2g} \int_0^{t_{\max}} a(t)^2 dt \quad (1)$$

where $a(t)$ is the ground acceleration at time t and t_{\max} is the total duration of the seismic signal. In addition, the maximum frequency of the Fourier power spectra (f_{\max}) and the total amount of spectral energy in 10 Hz frequency bands (f_{band}), spanning from 0 to 1000 Hz, were extracted to characterize the spectral features of MS and false events.

In particular, the spectral energy in each frequency band was computed as:

$$E_{\text{band}_{f_0 \rightarrow f_0+10}} = \int_{f_0}^{f_0+10} \text{DFT}(f) df \quad (2)$$

where $\text{DFT}(f)$ is the value of the power spectrum at the frequency f , obtained through the discrete Fourier transform of the event signal. Another important task that should be performed when dealing with MS analysis is related to the location of event sources. For what concerns this work, event location was not conducted because it was found to be not possible for different reasons. Since the two adopted array configurations were organized in a very restricted space, no delays in the arrival time of MS events were identified on the different channels, even considering the high sampling frequency adopted (i.e., 2400 Hz). For this reason, an attempt was made to retrieve information on microseismic activity sources by compiling a modified frequency–magnitude curve according to the Gutenberg–Richter power law [59]:

$$\log_{10} N = a - bM \quad (3)$$

where N is the cumulative number of events having a magnitude higher than M , while a and b are constants. Given the already discussed impossibility of locating MS events and due to the lack of information on their magnitude, the frequency–magnitude relation was modified by considering the I_A . In fact, this parameter is characterized by a log-linear relation to the moment magnitude (M), as empirically verified by Wilson [60], with strong motion data from several California earthquakes:

$$\log_{10}(I_A) = M - 2 \log_{10}(R) - 3.99 \quad (4)$$

where I_A is the Arias intensity, M is the moment magnitude, and R is the distance from the seismic source. Considering the linear relationship between M and the logarithm of I_A , and assuming that R is equal for all recording stations, the frequency–intensity curves were derived as follows:

$$\log_{10} N = a - b \log_{10}(I_A) \quad (5)$$

The most significant parameter of the equation is the b -value, which can vary strongly depending on the predominant failure mechanism at the source [38]. Even though this approach can be considered non-canonical, it was regarded as the only possible way to acquire information on potential microseismicity sources. Moreover, the same frequency–intensity curve and the related power law were also computed considering false events. This step allowed us to produce a comparison with the MS frequency–intensity curve and to test whether any difference could be noticeable. Based on the results obtained from the event classification, the temporal evolution of microseismicity was investigated by exploring potential correlations with multiple environmental factors (i.e., daily and seasonal temperature fluctuations, thermal gradients, and rainfall) to highlight the influence of such stresses in controlling the stability of the monitored rock mass.

4. Results

4.1. Analysis and Preliminary Classification of the MS Dataset

The results obtained using the STA/LTA algorithm are presented in Figure 5, where the raw number of triggered events is plotted. During the first monitoring campaign (February 2018–May 2018), 507 events were detected, while only 357 were extracted from the second campaign (November 2018–October 2019). From the observation of the detected events during the considered monitoring periods, different rates and trends (Figure 5a,b) in the occurrence of the events could be discerned. This evidence may be a consequence of the different array configurations employed during the two monitoring windows. By considering the different spacings between the two array configurations and the potential attenuation of seismic waves due to the presence of discontinuities, a dense array such as the one arranged from February 2018 to May 2018 may have the ability to detect a higher number of events common for different channels (Figure 5c,d). In Figure 5e, the distribution of the 864 triggered events is described in terms of the hour of the day in which they occurred. Interestingly, while the events belonging to the first monitoring campaign tend to be distributed almost homogeneously during the day, with no isolated peaks, the second monitoring campaign is characterized by a suspicious maximum between 11:00 and 12:00. This outcome may be in part biased by the almost complete absence of events during the night hours for the second monitoring period. In fact, as previously introduced, the monitoring system suffered from recurrent interruptions of the power supply from after sunset to some hours after sunrise (Figure 5f).

Following the automatic extraction of signals from the continuous recordings, the derived dataset was classified through a manual screening to exclude false detections from the analysis of the local microseismicity. The manual classification was performed by observing waveforms, power spectra, and spectrograms of every array channel (Figure 6). This technique is widely considered one of the fastest and most accurate methods for concurrently analyzing the time- and frequency-domain characteristics of signals [21]. This analysis led to the identification of multiple recurrent types of events. For the aim of this work, the event classification was performed between only two classes: the first one clustered all evident disturbances that could not be considered as natural events, and the second one comprised all the signals potentially related to the stability conditions of the monitored rock mass and rock block. Differently from several authors [8,21,29], within the latter class no further classification was made because it was not considered essential for the objective of this analysis.

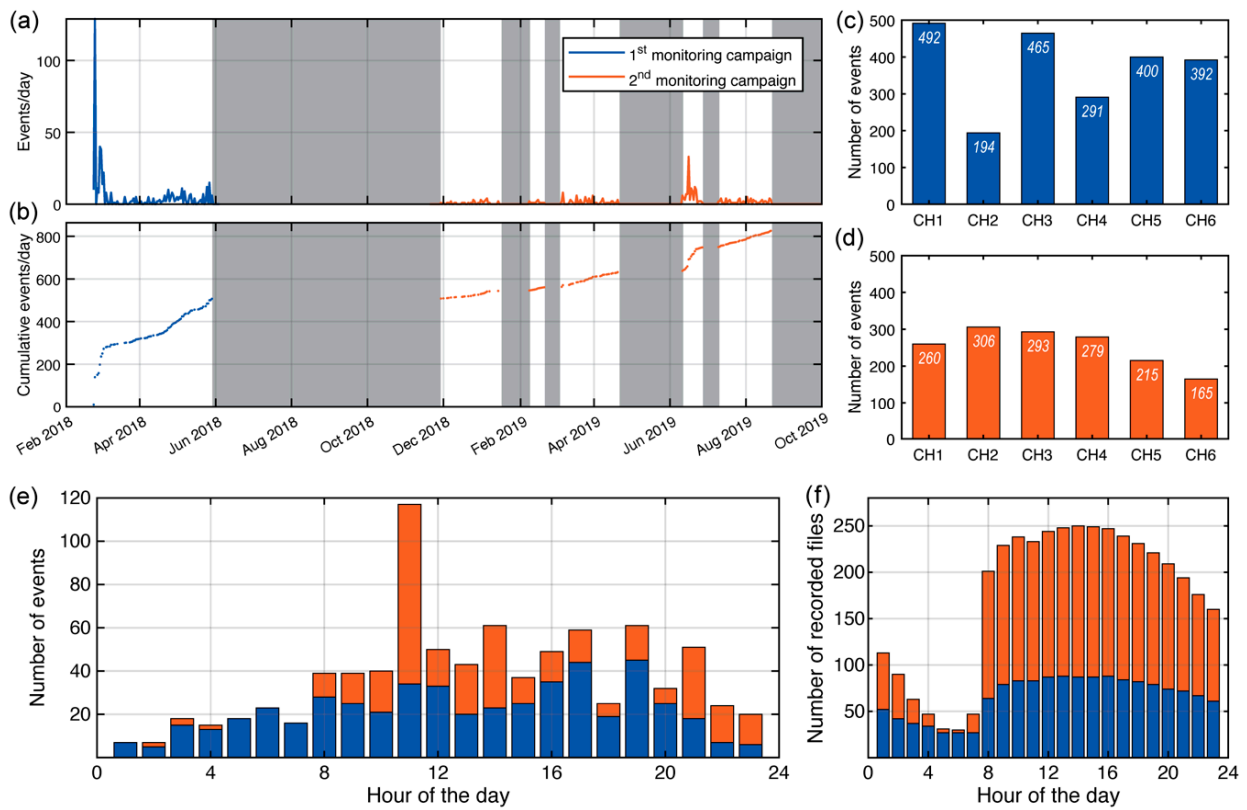


Figure 5. MS dataset collected at the Acuto field laboratory during the two monitoring campaigns conducted between February 2018 and October 2019. Number of events per day (a), cumulative number of events (b), and number of events detected per accelerometers during the first (c) and second monitoring campaign (d). Distributions of the detected events (e) and of the 1 h recorded files (f) during both monitoring campaigns as a function of the hour of the day.

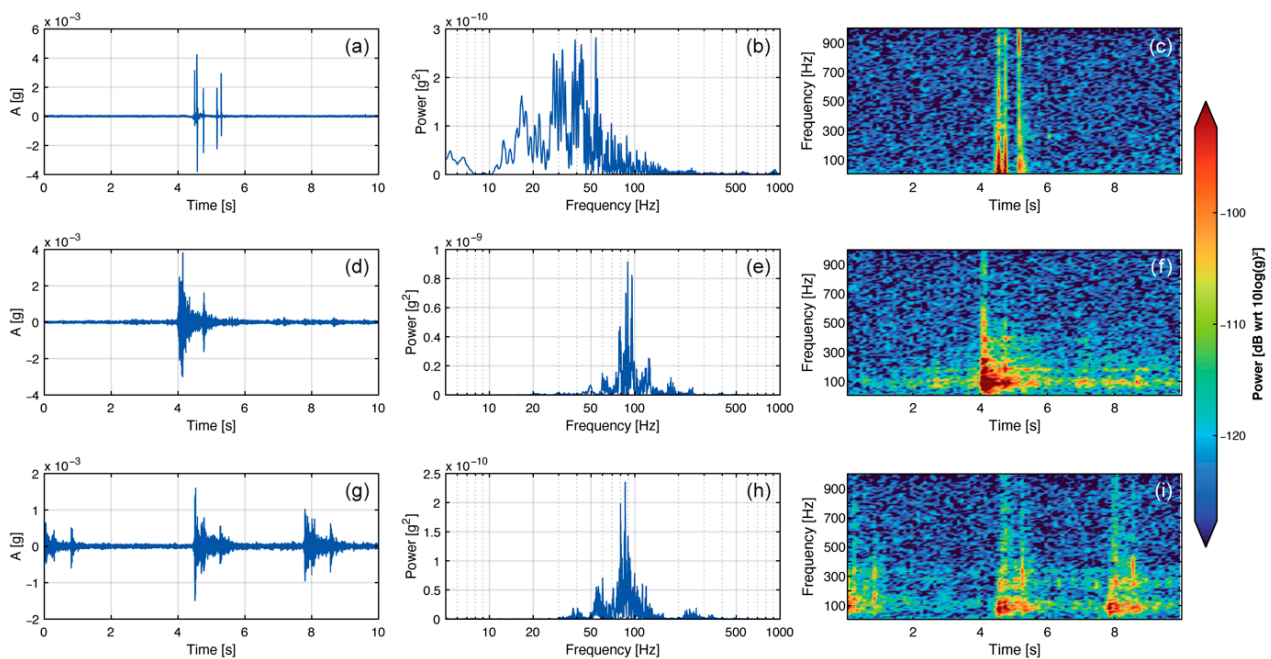


Figure 6. Example of electrical disturbances recorded at the Acuto field laboratory and manually classified as false events (a–c); example of a manually classified single MS event (d–f); example of a manually classified sequence of MS events (g–i).

The results of the manual classification highlighted that the MS monitoring network was affected by frequent electrical disturbances. These electrical transients simultaneously appear on all channels as single or multiple impulsive spike-like signals (Figure 6a–c) and are either characterized by a very broadband frequency content or by narrow frequency peaks systematically located above 200 Hz. The origin of these events is controversial, but they are considered to be caused by atmospheric electromagnetic transients or other electrical disturbances affecting the entire acquisition system [8,32]. Within the analyzed dataset, a total number of 591 electrical transients were identified (68% of the dataset) and classified as false events. The remaining 273 events, manually classified as MS events, show common recurrent time- and frequency-domain features. These events are characterized by short durations (from less than a second up to a few seconds), impulsive onsets, and a well-defined triangular envelope shape (Figure 6d–f). Their spectral range is concentrated between 30 and 150 Hz, and they were found to occur singularly and in short duration sequences (Figure 6g–i). Several authors have recognized these features as being typical of MS events [8,15,21]. In particular, the triangular shape of spectrograms can be interpreted as caused by the attenuation of higher frequencies due to the presence of dense discontinuity networks [8].

During the entire monitoring period, only one small-size rockfall (1 m³ ca.) occurred in the area close to the monitored rock block (between 9–11 March), but no signals were recorded because the monitoring network was not functioning due to a power interruption [18]. Similarly, no evidence of local earthquakes occurring within a radius of 50 km was found in ambient noise recordings over the whole monitoring period [22]. Nevertheless, even though the analyzed dataset was composed of less than one thousand events, the manual classification might still have been affected by some uncertainties as it was highly dependent on a subjective selection.

To evaluate the goodness of the manual classification, a quantitative comparison between the two identified classes was performed by analyzing several characteristic time- and frequency-domain parameters of the signals. In Figure 7, each panel compares couples of parameters that were considered for the investigation of the two clusters. The analysis of the relationship between kurtosis and event durations (bracketed and uniform) highlights how false events are concentrated in the left region of both plots (Figure 7a,b), thus confirming their very short and impulsive onset. In contrast, MS events show distributions characterized by variable durations. This behavior could be derived from the fact that both single events (uniform duration > 1–2 s) and sequences of multiple events (bracketed duration > 3–4 s) coexist within this class. The most evident difference between the kurtosis values of these clusters is the broader variability that characterizes the class of false events, with values ranging from 10¹ up to more than 10³ (Figure 7a,b). Since the kurtosis of the envelope describes the flatness or peakedness of a random variable distribution compared to a normal distribution, high values of this parameter are expected for impulsive transients, while low values are typical of background noise [21,55]. By observing the almost linear relationship between the normalized maximum amplitude (A_{\max}/A_{mean}) and the Arias intensity (I_A), two distinct alignments of MS and false events are evident (Figure 7c), with the latter class characterized by higher A_{\max}/A_{mean} values than the former within the same interval of I_A . In addition, a clear cluster of false events is concentrated at very low A_{\max}/A_{mean} and I_A values, probably describing noise transients rather than energetic electrical disturbances. Along with these results, the most significant differences observed between the two manually identified classes are shown in panels d and e of Figure 7. In these plots, the spectral content of all events, represented both in terms of peak frequency (f_{\max}) and 10-Hz frequency bands (f_{band}), was compared to their A_{\max}/A_{mean} values. The cluster of MS events is characterized by a frequency range spanning between 40 and 110 Hz, while the cluster of false events exhibits a bimodal distribution with two isolated local maxima located at very low (<10 Hz) and very high frequencies (>300 Hz). A synthesis of the eight parameters considered for comparing the identified classes of events is presented in Figure 8. As previously stated, the objective of this analysis was to produce a comparison between MS and false events

that could strengthen the outcomes of the manual classification through the investigation of characteristic time- and frequency-domain features.

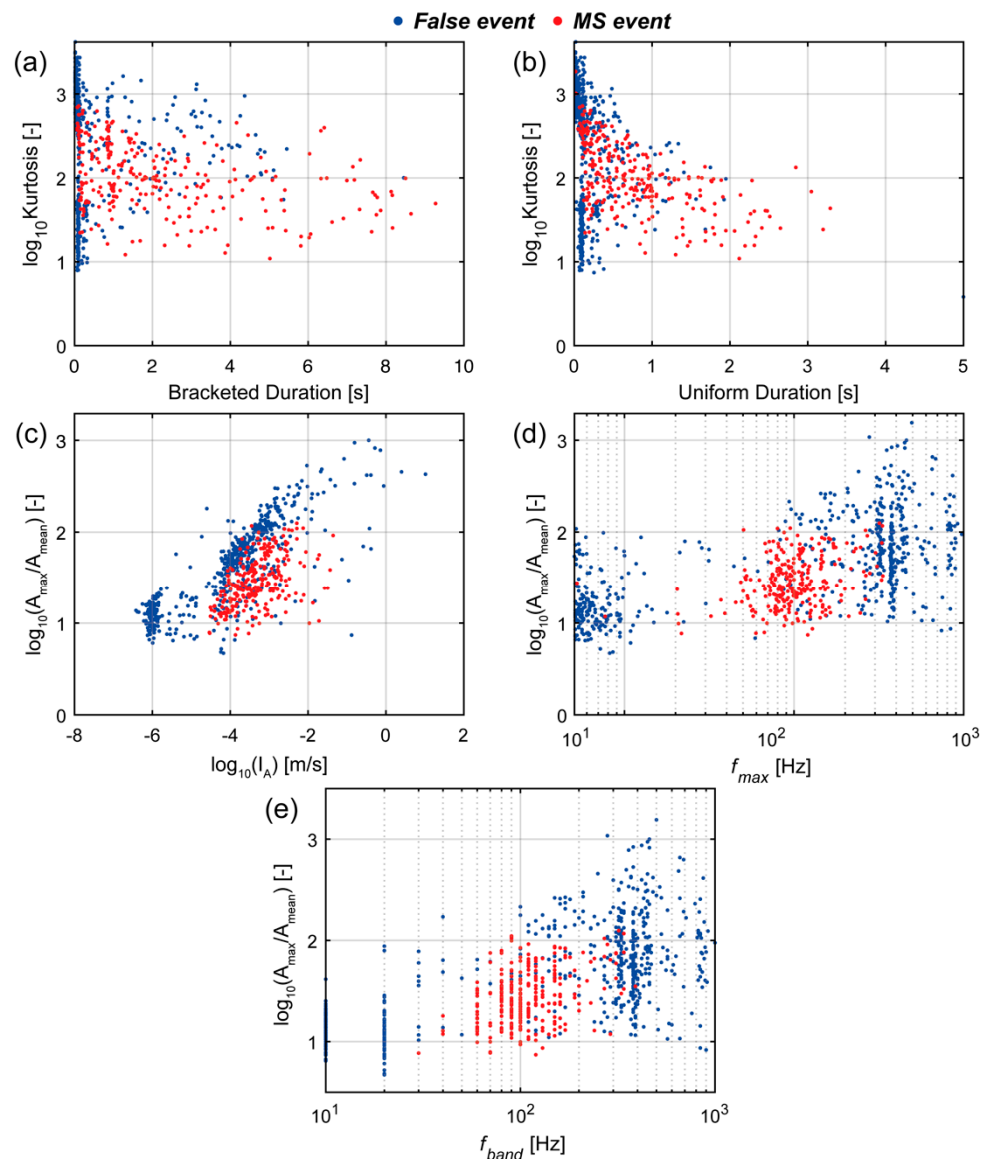


Figure 7. Results of the comparison between manually classified false and MS events based on time- and frequency-domain features. The following plots are presented: kurtosis vs. bracketed duration (a), kurtosis vs. uniform duration (b), maximum amplitude normalized to the mean of the envelope of the signal (A_{\max}/A_{mean}) vs. Arias intensity (I_A) (c), A_{\max}/A_{mean} vs. the frequency peak of power spectra (f_{\max}) (d), and the 10-Hz frequency band with the maximum spectral content (f_{band}) (e).

Based on the obtained results and considering MS and false events as two separate clusters, the relationship between event frequency and intensity was analyzed for both clusters according to the modified Gutenberg–Richter power law (Equation (5)). Due to the impossibility of locating event sources and estimating their magnitudes, these frequency–intensity curves were built considering the cumulative number of events having I_A values greater than a certain I_A . Their b-values were computed through linear regression (Figure 9). From the obtained results, which can be considered to be statistically significant in virtue of the high values of R-square (~ 0.98), the two clusters are characterized by different frequency–intensity distributions having b-values of 0.69 (MS events) and 0.46 (false events).

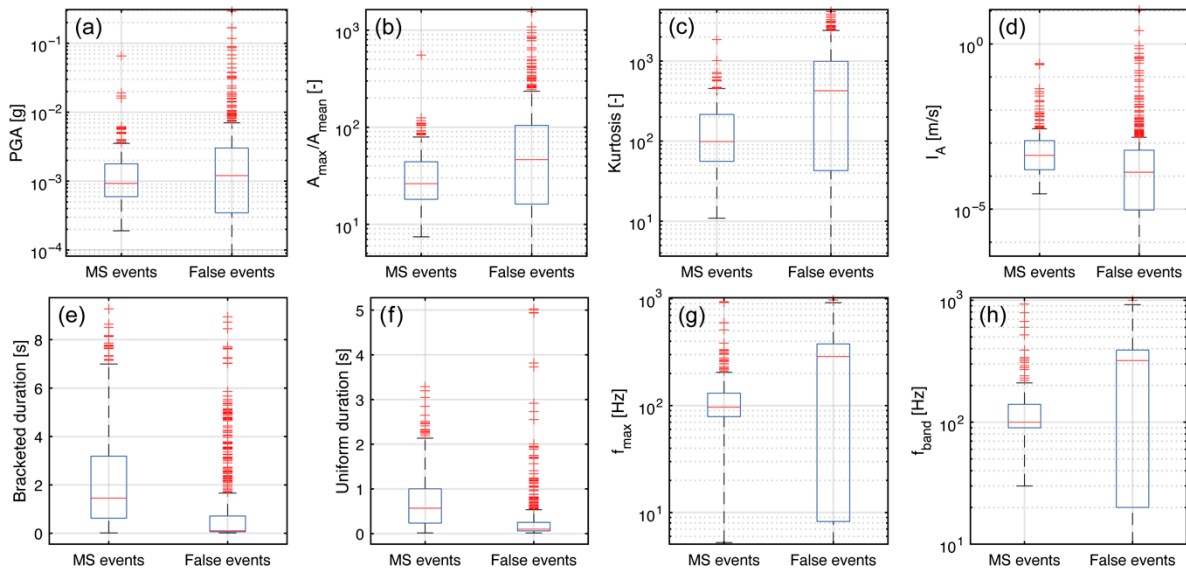


Figure 8. Synthesis of the statistical comparison between the two manually identified classes of detected events. For each class, the extension of the blue boxes represents the interquartile range (IQR, defined as the difference between the upper (Q3) and lower (Q1) quartiles), red lines are median values, black whiskers extend to extreme values, and red crosses are the not-considered outliers. The parameters considered for this analysis are PGA (a), normalized amplitude (b), kurtosis (c), Arias intensity (d), bracketed (e) and uniform duration (f), peak frequency (g), and most energized frequency band (h).

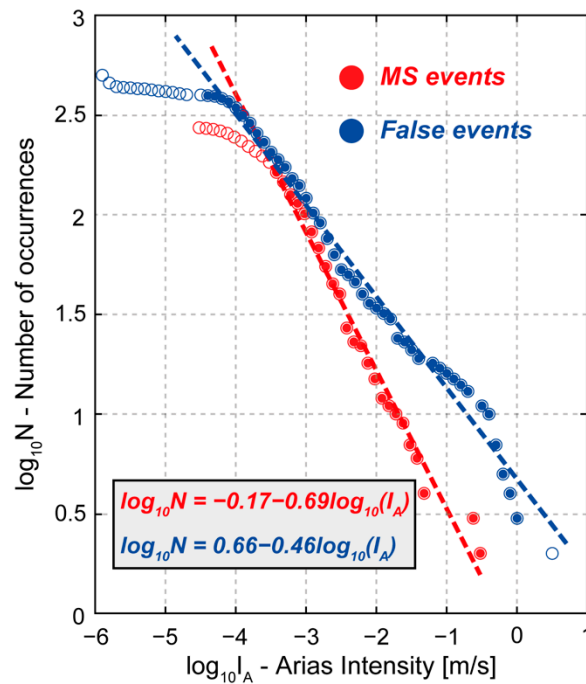


Figure 9. Comparison between the logarithm of Arias intensity (I_A) and the logarithm of the cumulative number of occurrences (N) for MS events and false events, following the modified Gutenberg and Richter (1954) power law relation.

Although one of the main goals of reconstructing frequency–intensity distributions for earthquakes is the characterization of seismic sources and the failure mechanism, since different b -values can be considered as source-specific [38,61], no inferences can be proposed here in terms of source or failure mechanism assessment. However, the

observed differentiation between frequency–intensity distributions of MS and false events is interpreted as an element that further corroborates the goodness of the manual classification process. Even though these results are insufficient to constrain and characterize the source of MS events, this analysis can be considered to be a preliminary attempt to gain valuable insights to distinguish possible source mechanisms responsible for the local microseismicity.

4.2. Correlation of MS Events with Environmental Factors

By observing the cumulative curves of MS and false events for the entire monitoring period, different trends in the occurrence of these two classes are evident (Figure 10). Although both curves show increasing rates during periods with similar climatic and weather conditions (P1, P2, P3), the occurrence rate of false events is significantly higher than the rate of MS events. Moreover, another peak in the event occurrence is found in the absence of rainfall and significant temperature fluctuations (P4). As already discussed, this effect can be interpreted as being derived from the influence of meteorological factors on the onset of frequent electrical disturbances. However, it must be noted that even MS events do not show negligible increasing rates during the same time intervals, except for P3. The analysis of the temporal evolution of the MS events highlighted the existence of several days in which more than five events occurred (Figure 10c). These peaks mostly clustered during the period between February and April 2018, when 63% of all events were detected. The highest peak in the daily distribution of MS events (32), which is also preceded and followed by days of intense MS activity, is located within a time window characterized by a sharp decrease in rock mass temperatures and consistent rainfalls/snowfalls. At the end of February 2018, the entire region of Central Italy experienced an extreme meteorological event due to an incoming perturbation associated with the buran, a cold north-easterly wind that is typical of the steppes of the Siberian region [17]. At the Acuto field laboratory, air and rock mass temperatures reached their minimum values of $-7.7\text{ }^{\circ}\text{C}$ and $-3.8\text{ }^{\circ}\text{C}$, respectively, and almost 106 mm of rainfall occurred within a 7-day time interval. The sharp temperature decrease caused freezing conditions that remained stable for four days (from 25 February 2018 to 1 March 2018). This winter storm was responsible for a short and intense thermal transient in the seasonal temperature trend, representing an unprecedented event in the seven-year environmental monitoring dataset collected at the Acuto field laboratory (2015–2022).

Apart from this short-term variation in the environmental boundary conditions that caused a significant acceleration in the occurrence of MS events, with 83 MS events concentrated in 12 days, other isolated MS peaks can be observed in Figure 10, especially during April 2018 (8 MS events on 24 April 2018), May 2018 (12 MS events on 27 May 2018), and June 2019 (16 MS events on 19 June 2019 and 7 MS events on 22 June 2019). However, their correlation with external continuous (i.e., thermal variations) and transient (i.e., rainfalls) stresses is not as straightforward as for the period in which the rock mass experienced freezing conditions. Unfortunately, it must be stated that due to the limited number of MS events collected during the discontinuous 20-month MS monitoring, a statistical analysis aimed at deepening the correlations between rainfall, temperature fluctuations, and the occurrence of MS events, as suggested by Helmstetter and Garambois [43] and Arosio et al. [8], was not performed. To achieve preliminary insights into potential cause-and-effect relationships between the abovementioned factors, the analysis of the temporal evolution and distribution of MS events was approached by employing an observational-based approach. An attempt to investigate the influence of temperature fluctuations on the local MS activity was made by analyzing the distribution of MS events during the heating and cooling phases of the rock mass (Figure 11). To this aim, the heating and cooling ramps of rock temperature timeseries were analyzed, and the minimum and maximum recorded values were extracted along with their average duration for each day of the monitoring period. Therefore, MS events were classified according to the ramp in which they occurred to highlight any recurrent pattern in their distribution on the daily timescale.

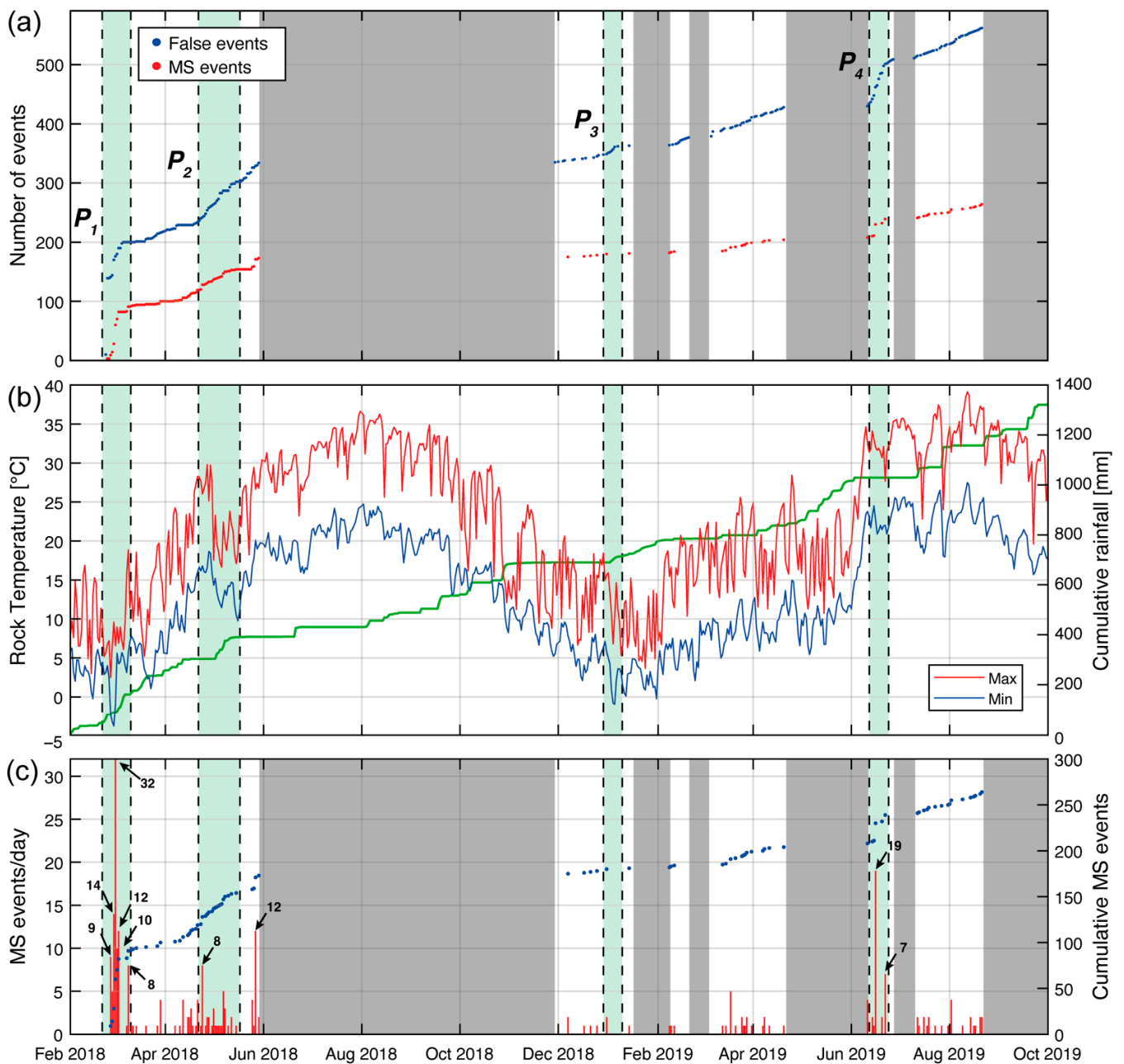


Figure 10. Comparison between the temporal evolution of MS events and environmental factors at the Acuto field laboratory: cumulative number of MS and false events computed over the entire monitoring period (a); daily maximum–minimum rock temperature (red and blue lines) and cumulative rainfall (green line) (b); daily and cumulative number of MS events (c). Four time intervals (P_1 – P_2 – P_3 – P_4) are highlighted in all plots representing the periods in which the highest increments in both MS and false event occurrence were observed. Gray areas in panels (a,c) represent periods in which the MS monitoring network was not working due to power supply interruptions.

The amplitude of temperature ranges was then computed for each cooling ramp as the difference between the maximum daily temperature and the subsequent minimum, while for heating ramps they were computed in the opposite way (Figure 11b). Furthermore, the mean rate of rock mass heating and cooling ramps was computed by dividing their amplitude by their duration (Figure 11c).

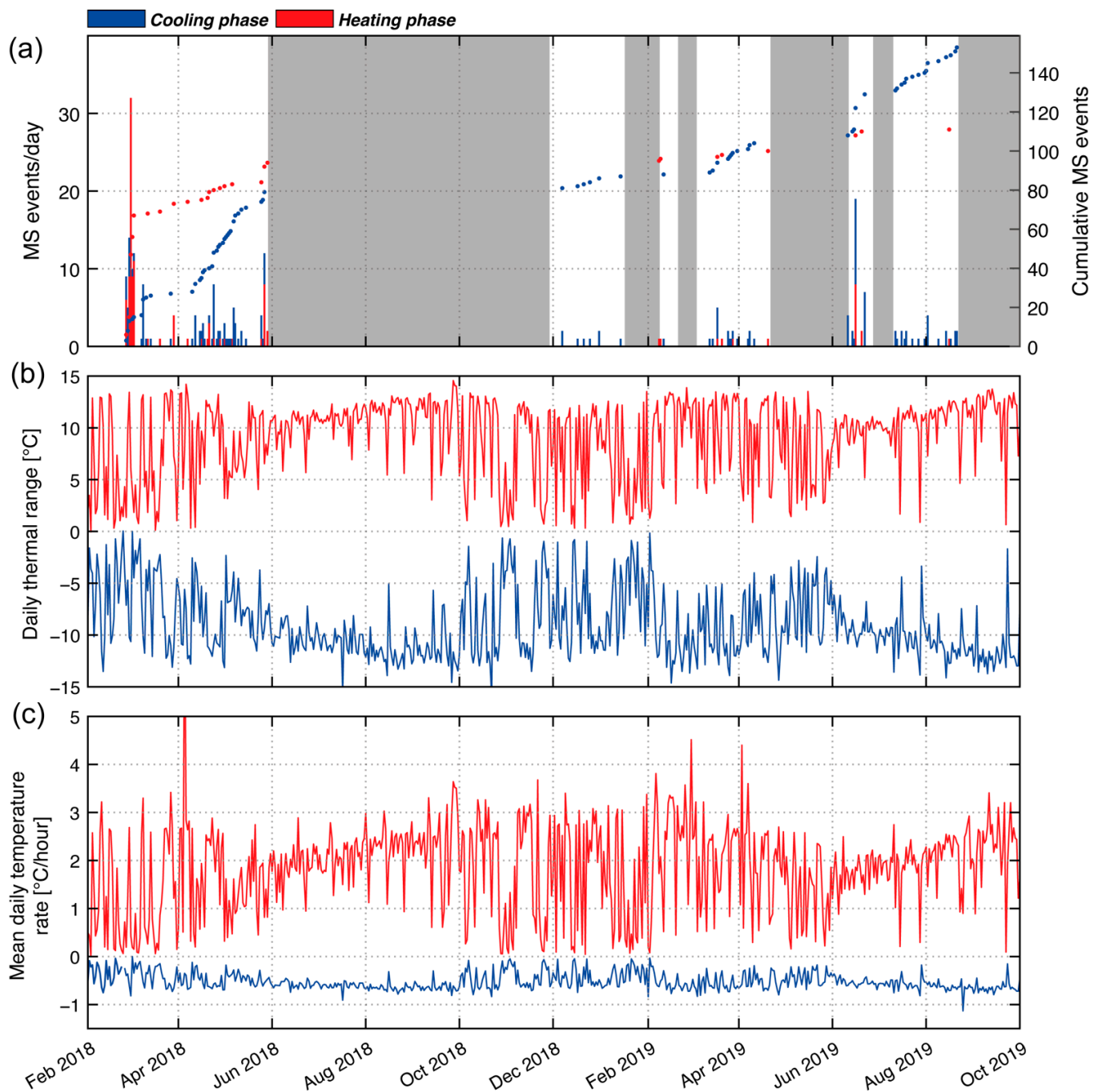


Figure 11. Comparison between the distribution of MS events (a), daily thermal ranges (b), and mean daily temperature rates (c). In each plot, the distinction between the heating (in red) and cooling (blue) phases of the rock mass is proposed with a view to investigate the response of the jointed rock block to different thermal regimes of increasing (heating) or decreasing (cooling) temperatures. Gray areas in panel (a) represent periods in which the MS monitoring network was not working due to power supply interruptions.

MS events show a clear differentiation in their distribution between the heating and cooling phases, with 111 and 153 MS events, respectively. In more detail, during the 4-day freezing period of February 2018, 69 MS events occurred in correspondence with an increasing temperature regime (i.e., heating phase), while only 14 of them were recorded during a regime of decreasing temperatures, meaning that 63% of all MS events that occurred during cooling phases were clustered during this extreme meteorological transient.

The magnitude of temperature ranges of heating and cooling ramps is comparable, also showing a significant variability throughout the entire period, but the average rates of heating ramps are consistently higher than the cooling ramps. On the contrary, if excluding the period characterized by not-common weather conditions (i.e., the winter storm), the microseismicity tends to be concentrated during the cooling phases of the rock mass, as also highlighted by the different trends in their cumulative curves (Figure 11a). However, since the MS dataset is affected by several month-long gaps, the comprehension of the relationship between thermal boundary conditions and the local microseismicity is difficult to discern. MS events show a very discontinuous distribution during the whole monitoring period with a limited number of short time windows in which a significant concentration of MS events is recorded. For this reason, a detailed investigation of three distinct periods characterized by the highest MS event peaks was performed. These periods were selected as they were also representative of different climatic and meteorological conditions. For each time window, the comparison between rainfall intensity, temperature fluctuations, and MS event distribution was performed with a view of highlighting the influence of highly variable environmental conditions on the potential acceleration of fracturing processes (Figure 12). The first period comprises a time window spanning from 23 February 2018 to 14 March 2018 when, as previously introduced, the quarry area experienced an unprecedented weather event (Figure 12a–c). In this period, the most intense MS activity is clustered in four days characterized by a marked temperature drop that caused freezing conditions and by a small amount of cumulated rainfalls (Figure 12a). MS events seem to be better correlated to temperature variations rather than to rainfalls. This evidence is also strengthened by the almost-perfect correlation between the 1 h rate of event occurrence and the evolution of daily temperature ranges and 1 h temperature rates, with the absolute highest MS peak (32 events) occurring immediately after a day characterized by a 14.5 °C daily thermal excursion and a maximum temperature rate of 4 °C/h (Figure 12b). Furthermore, the occurrence of MS events during the winter storm appears to be clustered during the heating phases of the rock mass.

It must be considered that the scarce correlation between MS events and rainfalls during this time interval may be in part biased by the fact that the rain gauge mostly measured snow melt. In fact, the weather station was not equipped with a nivometer and, since the quarry was completely covered by snow during these days, the analysis of the correlation between MS events and rainfalls could not be thoroughly investigated. Nevertheless, after the end of the buran storm, a significant increase in rainfall was observed between 5 March and 8 March, but no MS events were recorded, except for an isolated peak that was triggered and characterized by a delay of two days. This evidence highlights that the microseismicity observed during the freezing period is more likely related to the rapid decrease and increase in near-surface temperatures.

Thermally induced stresses are in fact able to drive differential strain variations, especially in the outermost layers of rock masses, where their amplitude is highest, resulting in contraction and expansion cycles of fractures and microfractures that can eventually lead to their genesis or propagation [19,44,62].

In addition, if considering the amount of rainfall that occurred before the winter storm, a freezing and thawing mechanism may also be invoked to justify the numerous MS events detected during this short time interval. The persistent freezing conditions might have favored the formation of ice inside fractures and microcracks during the cooling phases of the rock mass, leading to the accumulation of inelastic strain at the tip of discontinuities [63]. Then, the rise in temperatures during the first stages of the heating phases, driven by high positive thermal gradients, might have caused the rapid ice melting followed by a consequent stress release that could be considered the primary cause of the intense MS activity. This evidence is limited to this time window which is characterized by extreme and non-representative conditions of the normal climatic setting of the Acuto quarry area.

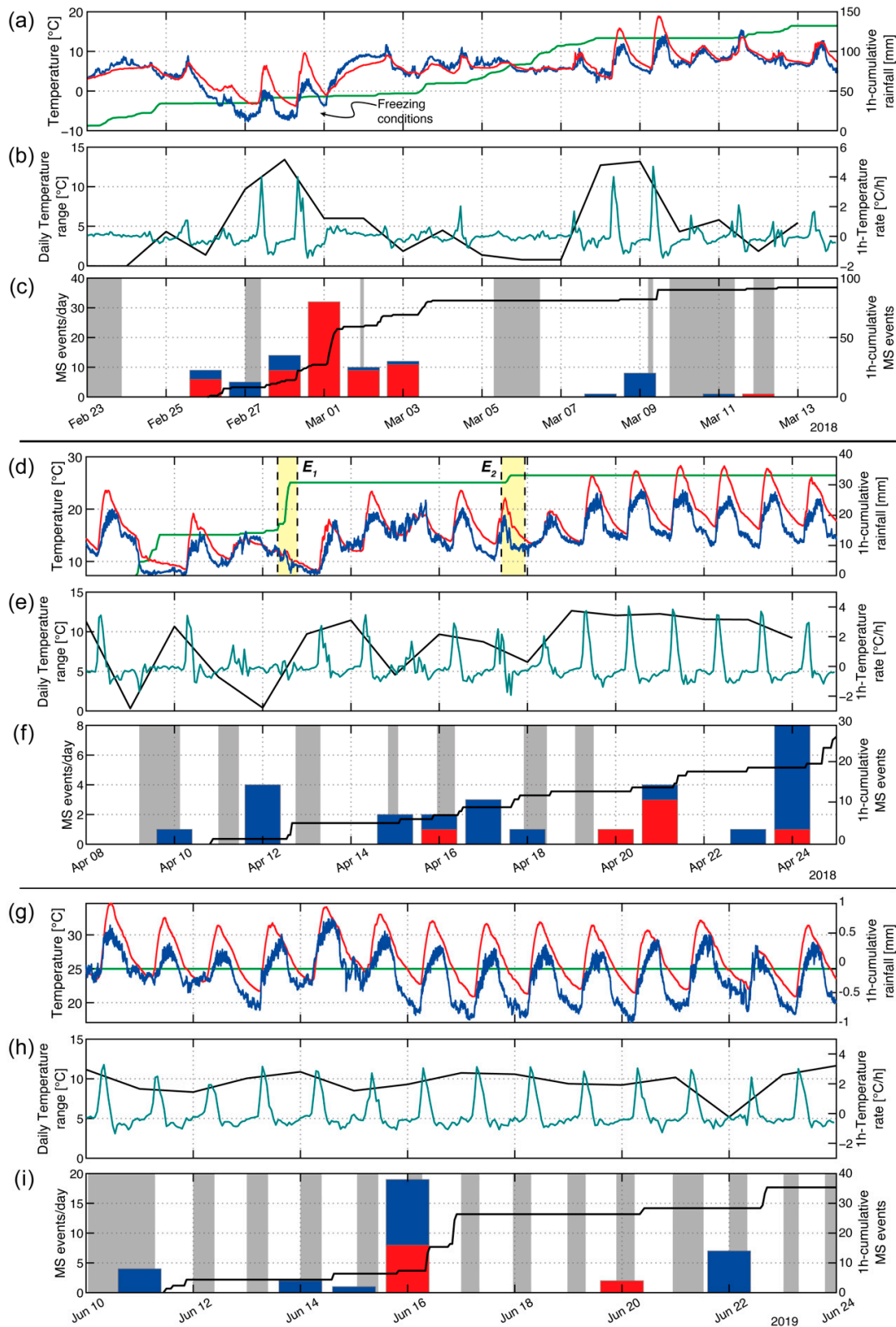


Figure 12. Comparison between environmental factors and the occurrence of MS events for the periods between February 2018 and March 2018 (a–c), and April 2018 (d–f) and June 2019 (g–i): 10 min air (blue line), rock mass temperature (red line), and 1 h cumulative rainfall (green line) (a,d,g); daily temperature range (i.e., thermal excursion) (black line) and 1 h rock temperature rate (blue line) (b,e,h); daily distribution of MS events occurred during the heating phase (red bars) and cooling phase (blue bars) of the rock mass along with the 1 h cumulative MS events curve (black line) (c,f,i).

The other two investigated periods are instead more representative of the environmental boundary conditions of the area. For example, during the second period spanning from 8 April 2018 to 25 April 2018, 29 MS events were detected, but this value is certainly underestimated due to the periodic interruption of the MS monitoring system at night (Figure 12d–f). Near-surface temperatures show a decreasing trend during the first days (from 8 April to 13 April) that is related to a minor meteorological perturbation which caused temperature rates and gradients to significantly vary (Figure 12e). One of the most distinct features of this monitoring interval with respect to the winter storm is represented by the higher correlation that can be found between MS events and rainfalls, rather than with temperature fluctuations. Two rainfall events characterized by different intensities (E1 and E2, Figure 12d) may be regarded as the primary causes of the MS events that occurred during and immediately after these rainfalls (Figure 12f), while daily temperature ranges and rates do not exhibit significant variations. The last days of this period are instead characterized by the absence of rainfalls and by a steady increase in MS events, with a maximum peak of eight events on 24 April 24 that are associated with an increasing trend of temperatures which determined the stabilization of high temperature ranges and rates.

Similar conditions are found in the period ranging between 10 June 2019 and 24 June 2019 that is representative of typical warmer climatic conditions characterized by the complete absence of rainfalls (Figure 12g). Here, MS events cannot be correlated with rainfalls and their occurrence is more likely caused by the continuous effect of daily thermal cycles. From the observation of the 1 h cumulative occurrence of MS events, three peaks are particularly apparent and mostly clustered during the cooling stages of the rock block (Figure 12i). The higher concentration of MS events during periods characterized by rapid temperature variations (i.e., high temperature rates), and especially during cooling phases, agrees with what has already been observed by several authors in different case studies [19,63].

5. Discussion

The availability of a vast dataset consisting of almost 5000 h of continuous ambient noise recordings allowed us to calibrate STA/LTA triggering algorithm parameters efficiently. Since several analyses had already been conducted on part of the here-discussed monitoring data [18,23,24], it was possible to optimize the event detection algorithm from the results obtained by D'Angiò [23]. In their framework, a total number of 115,000 events were detected employing the same STA/LTA algorithm with different settings ($STA = 0.01$ s, $LTA = 30$ s, $STA/LTA = 4$, and $N_{Th} = 2$) over a period spanning from February 2018 to April 2019. The results obtained by D'Angiò [17] were considered valid in terms of the number of detections, but no manual or automatic event classification was performed on the extracted signals because it was considered not relevant for the final objective of their work. Although, when investigating potential correlations between MS activity and environmental factors (i.e., rainfalls and temperature variations), the consideration of false events could vitiate the outcomes, especially when they may represent the great majority of the dataset. For this reason, to reduce the number of detections within the considered monitoring periods and at the same time avoid significant losses in information, the STA/LTA algorithm settings were calibrated on a training dataset of several months. The most significant difference between the here-proposed parameters and those adopted in previous studies is represented by the size of the STA window and the selected value of N_{Th} . In this study, they were increased to reduce the algorithm's sensitivity to very short and low-coherence signals.

The semi-automatic approach adopted for the detection and classification of waveforms led to the construction of an MS dataset comprising 273 MS events over the 20-month monitoring period. As previously described, the monitoring dataset is affected by several issues, among which the most impactful are surely the presence of periodic time gaps in recordings, the limited number of detected MS events, and the impossibility to locate the events inside the rock mass. The lack of information concerning the genesis of MS events is

derived from the poor geometry of the monitoring array which did not permit finding the location of their sources. Therefore, some uncertainties related to their origin still remain and cannot be completely neglected. Nevertheless, the statistical analysis performed on the manually identified classes of events allowed us to reliably consider the identified MS events as indicators of irreversible deformations deriving from fracturing processes of the rock mass. Based on the available data, the conducted analyses provided a deeper understanding of the role played by continuous near-surface temperature fluctuations and extreme thermal transients in influencing the stability of the fractured rock block. Although the limited number of event detections did not provide an opportunity to perform a robust statistical analysis between environmental stressors (e.g., rainfalls and temperature fluctuations) and microseismicity, some interesting inferences could still be derived from the obtained results. One of the most interesting outcomes that emerged from the comparison between the above-presented monitoring periods is probably the different distribution of MS events during the heating and cooling phases of the investigated rock mass. Although the analyzed dataset is also affected by numerous time gaps and by a limited number of MS events, the temporal distribution of MS activity registered in average climatic conditions (second and third periods—Figure 12d–i) is mostly concentrated in the cooling phases of the rock mass, contrary to what was observed during the winter storm of February 2018. The plots of Figure 13 clearly summarize this differentiation between MS event distributions, showing that if excluding the winter storm of February 2018 from the analysis, more than 70% of all detected events occurred during the cooling phases of the rock mass (Figure 13). These behaviors can be interpreted as the consequence of different driving mechanisms at the base of local failure. For what concerns the transient and extreme meteorological perturbation (i.e., the buran storm) that caused the rock mass to experience freezing conditions, the combined effect exerted by ice formation inside fractures, freezing–thawing cycles, and high positive thermal gradients may have significantly contributed to the rapid acceleration of incipient fracturing processes (Figure 14a), as witnessed by the evident increase in the MS activity observed during the heating phases of a four-day time window.

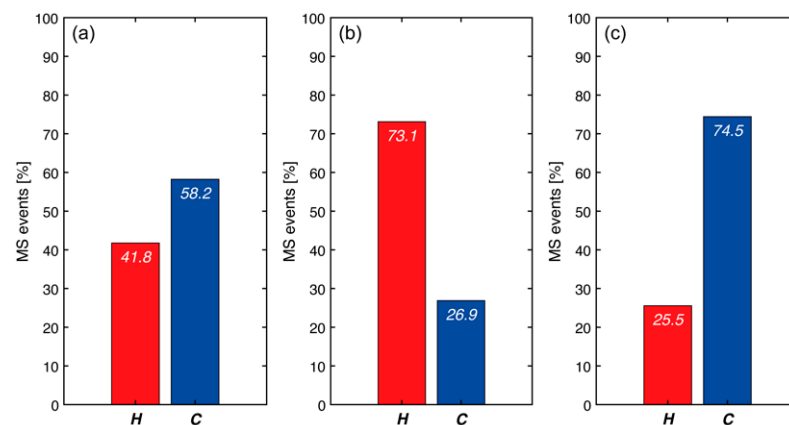


Figure 13. Percentage distribution of MS events during heating (in red) and cooling phases (in blue) for the whole monitoring period (a), the only winter storm of February 2018 (b), and for the entire monitoring period excluding the winter storm (c).

Conversely, in the absence of brief and violent meteorological events, the occurrence of MS events could be interpreted as the response of a complex interaction between the intensely jointed rock block and the continuous fluctuations in near-surface thermal fields which may eventually cause cyclic expansion and the contraction of fractures and microcracks.

This mechanism could act as a thermal fatigue process able to drive a slow yet continuous accumulation of unrecovered deformations that, if exceeding yield thresholds of plastic deformations, could cause localized failures followed by the release of energy in the form of MS signals (Figure 14b).

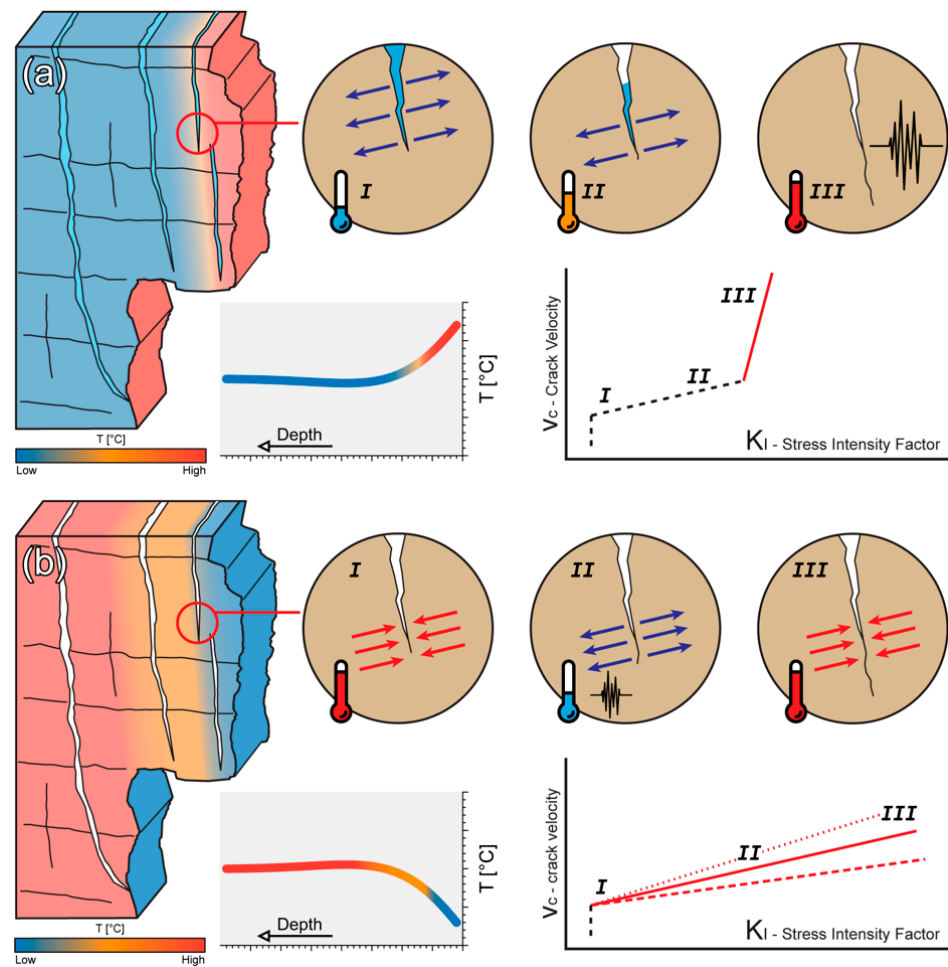


Figure 14. Conceptual model of the different thermally driven mechanisms interpreted as primary causes of the observed microseismicity at the Acuto field laboratory. Ice expansion pressure on crack surfaces generated by ice formation (I) and freezing–thawing cycles (II–III) can trigger dynamic and very rapid crack opening or propagation, with the release of energy in the form of MS events, as also described by the plot of crack velocity (v_c) versus crack driving force expressed as the stress intensity factor (K_I) (a). Conversely, the continuous variation in thermally induced expansion and contraction cycles of the crack (I–III) due to near-surface temperatures can determine the slow opening and propagation of the crack, acting as a thermal fatigue process (b).

However, a clear cause-and-effect relationship between MS events and near-surface temperature fluctuations is not easy to discern, since several environmental factors actively exert their influence on the monitored rock block. For this reason, longer monitoring intervals comprising a higher number of MS detections are required to better isolate the contribution of continuous and transient factors to the destabilization of the investigated rock block. Nevertheless, the limited number of MS events recognized during the entire monitoring period might be related to the general stable conditions of the monitored rock block, as also witnessed by the absence of irreversible deformation trends of major fractures and microcracks (Figure 15).

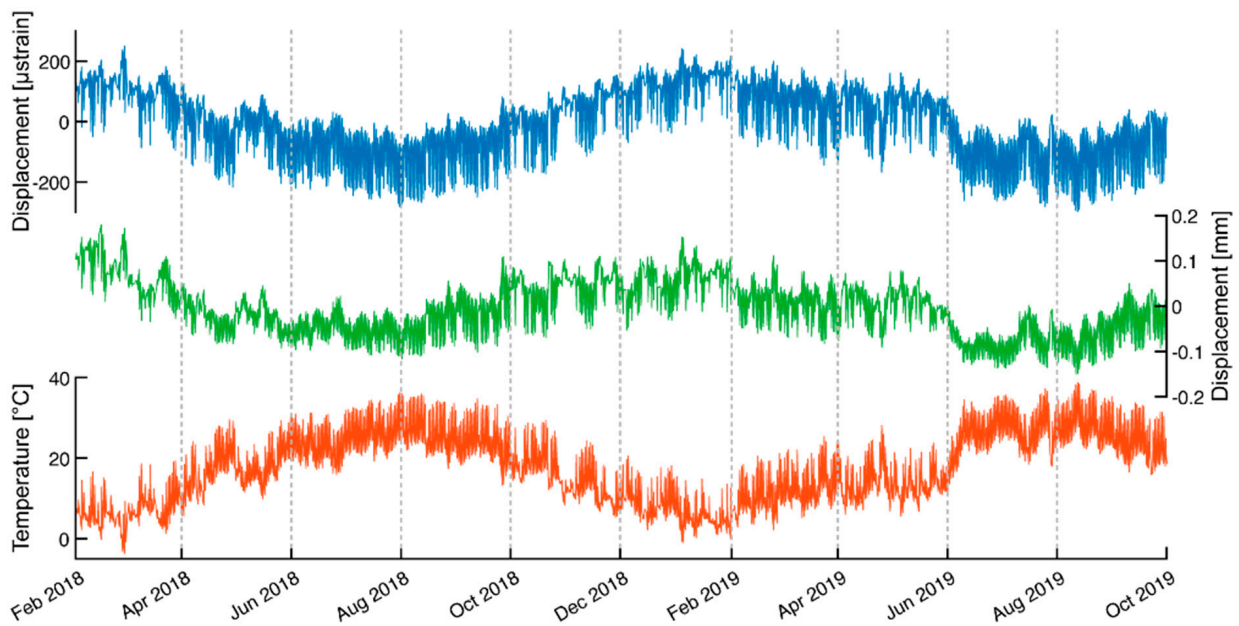


Figure 15. Temporal evolution of displacement (blue and green lines) and rock temperature (orange line) monitoring timeseries recorded by the permanent multiparametric monitoring system at the Acuto field laboratory.

6. Conclusions

Thermally induced deformations are among the lesser studied factors that can directly control rock mass stability. The assessment of the role played by near-surface temperature fluctuations in “preparing” jointed rock masses toward prone-to-fall conditions represents a research topic that has acquired growing interest among engineering geology researchers over recent years. The main objective of this work was to provide novel insights into the role of near-surface temperature fluctuations in inducing irreversible deformations on jointed rock masses. A semi-automatic approach was implemented to identify clusters of fracture-related MS events over long-term monitoring windows. The proposed workflow allowed the detection and classification of energetic signals and the construction of a dataset of 273 MS events over a 20-month monitoring period. Despite some limitations, the statistical analysis performed on the dataset suggests that the manually classified MS events can be reliably considered as indicators of irreversible deformations resulting from fracturing processes in the rock mass. The comparison between microseismicity and environmental factors highlighted the primary role played by continuous near-surface temperature fluctuations and extreme thermal transients in inducing nonlinear deformations in the rock mass. Although a robust statistical analysis could not be performed due to data discontinuity, the comparison of monitoring periods characterized by the most intense MS activity sheds light on a peculiar distribution of MS events during the heating and cooling phases of the rock mass in relation to different environmental conditions. In this sense, MS events tend to cluster during the cooling phases of the rock mass when average climatic conditions are dominant. Conversely, their frequency dramatically increases during the heating phases when brief and violent meteorological events occur. This differentiation which characterizes the local microseismicity could be considered to be a direct consequence of distinct driving mechanisms at the base of localized small-scale failure events. Nonetheless, a clear cause-and-effect relationship between MS events and near-surface thermal fields is difficult to discern due to the concurrent influence of multiple environmental factors. For this reason, longer monitoring datasets with a higher number of MS events are needed to better comprehend the contribution of environmental factors to the destabilization of jointed rock masses.

Author Contributions: Conceptualization, G.G., D.D. and S.M.; methodology, G.G. and D.D.; software, G.G. and D.D.; formal analysis, G.G.; investigation, G.G.; resources, G.G., D.D. and S.M.; data curation, G.G.; writing—original draft preparation, G.G.; writing—review and editing, G.G., D.D. and S.M.; visualization, G.G.; supervision, S.M.; project administration, G.G., D.D. and S.M.; funding acquisition, G.G., D.D. and S.M. All authors have read and agreed to the published version of the manuscript.

Funding: This study is part of the Ph.D. research project of Guglielmo Grechi and was funded by the Department of Earth Sciences of the Sapienza University of Rome and CERI research center under the framework of the Ministry of University (MUR) “Departments of Excellence” project (2018–2022), which includes the Acuto field laboratory as an innovative natural test-site for landslide risk management (scientist responsible: Salvatore Martino; email: acutofieldlab.dst@uniroma1.it).

Institutional Review Board Statement: Not applicable.

Informed Consent Statement: Not applicable.

Data Availability Statement: Data and codes used in this study are available upon request from the corresponding author.

Acknowledgments: We wish to thank the reviewers of the Ph.D. thesis, Chiara Colombero and Jan Burjánek, for their remarks and valuable feedback; two anonymous reviewers for their constructive reviews which have greatly improved our manuscript; the Municipality of Acuto for supporting the activities in the quarry area; and Gian Marco Marmoni, Matteo Fiorucci, and Roberto Iannucci for their availability and unfailing commitment in organizing and performing the experimental field activities. Last but not least, we would like to thank Molly McCreary and Silvia Pettinato for their help and invaluable support.

Conflicts of Interest: The authors declare no conflict of interest.

References

1. Aldred, J.; Eppes, M.C.; Aquino, K.; Deal, R.; Garbini, J.; Swami, S.; Tuttle, A.; Xanthos, G. The Influence of Solar-Induced Thermal Stresses on the Mechanical Weathering of Rocks in Humid Mid-Latitudes. *Earth Surf. Process. Landf.* **2016**, *41*, 603–614. [[CrossRef](#)]
2. Bakun-Mazor, D.; Keissar, Y.; Feldheim, A.; Detournay, C.; Hatzor, Y.H. Thermally-Induced Wedging–Ratcheting Failure Mechanism in Rock Slopes. *Rock Mech. Rock Eng.* **2020**, *53*, 2521–2538. [[CrossRef](#)]
3. Bakun-Mazor, D.; Hatzor, Y.H.; Glaser, S.D.; Carlos Santamarina, J. Thermally vs. Seismically Induced Block Displacements in Masada Rock Slopes. *Int. J. Rock Mech. Min. Sci.* **2013**, *61*, 196–211. [[CrossRef](#)]
4. Collins, B.D.; Stock, G.M.; Eppes, M.C.; Lewis, S.W.; Corbett, S.C.; Smith, J.B. Thermal Influences on Spontaneous Rock Dome Exfoliation. *Nat. Commun.* **2018**, *9*, 762. [[CrossRef](#)] [[PubMed](#)]
5. Collins, B.D.; Stock, G.M.; Eppes, M.C. Relaxation Response of Critically Stressed Macroscale Surficial Rock Sheets. *Rock Mech. Rock Eng.* **2019**, *52*, 5013–5023. [[CrossRef](#)]
6. Gunzburger, Y.; Merrien-Soukatchoff, V.; Guglielmi, Y. Influence of Daily Surface Temperature Fluctuations on Rock Slope Stability: Case Study of the Rochers de Valabres Slope (France). *Int. J. Rock Mech. Min. Sci.* **2005**, *42*, 331–349. [[CrossRef](#)]
7. Hall, K.; Thorn, C.E. Thermal Fatigue and Thermal Shock in Bedrock: An Attempt to Unravel the Geomorphic Processes and Products. *Geomorphology* **2014**, *206*, 1–13. [[CrossRef](#)]
8. Arosio, D.; Longoni, L.; Papini, M.; Boccolari, M.; Zanzi, L. Analysis of Microseismic Signals Collected on an Unstable Rock Face in the Italian Prealps. *Geophys. J. Int.* **2018**, *213*, 475–488. [[CrossRef](#)]
9. Valentin, J.; Capron, A.; Jongmans, D.; Baillet, L.; Bottelin, P.; Donze, F.; Larose, E.; Mangeney, A. The Dynamic Response of Prone-to-Fall Columns to Ambient Vibrations: Comparison between Measurements and Numerical Modelling. *Geophys. J. Int.* **2017**, *208*, 1058–1076. [[CrossRef](#)]
10. Kleinbrod, U.; Burjánek, J.; Fäh, D. Ambient Vibration Classification of Unstable Rock Slopes: A Systematic Approach. *Eng. Geol.* **2019**, *249*, 198–217. [[CrossRef](#)]
11. Colombero, C.; Godio, A.; Jongmans, D. Ambient Seismic Noise and Microseismicity Monitoring of a Prone-to-Fall Quartzite Tower (Ormea, NW Italy). *Remote Sens.* **2021**, *13*, 1664. [[CrossRef](#)]
12. Colombero, C.; Comina, C.; Vinciguerra, S.; Benson, P.M. Microseismicity of an Unstable Rock Mass: From Field Monitoring to Laboratory Testing. *J. Geophys. Res. Solid Earth* **2018**, *123*, 1673–1693. [[CrossRef](#)]
13. Colombero, C.; Baillet, L.; Comina, C.; Jongmans, D.; Larose, E.; Valentin, J.; Vinciguerra, S. Integration of Ambient Seismic Noise Monitoring, Displacement and Meteorological Measurements to Infer the Temperature-Controlled Long-Term Evolution of a Complex Prone-to-Fall Cliff. *Geophys. J. Int.* **2018**, *213*, 1876–1897. [[CrossRef](#)]
14. Dietze, M.; Krautblatter, M.; Illien, L.; Hovius, N. Seismic Constraints on Rock Damaging Related to a Failing Mountain Peak: The Hochvogel, Allgäu. *Earth Surf. Process. Landf.* **2021**, *46*, 417–429. [[CrossRef](#)]

15. Lévy, C.; Jongmans, D.; Baillet, L. Analysis of Seismic Signals Recorded on a Prone-to-Fall Rock Column (Vercors Massif, French Alps). *Geophys. J. Int.* **2011**, *186*, 296–310. [[CrossRef](#)]
16. Starr, A.M.; Moore, J.R.; Thorne, M.S. Ambient Resonance of Mesa Arch, Canyonlands National Park, Utah. *Geophys. Res. Lett.* **2015**, *42*, 6696–6702. [[CrossRef](#)]
17. D’Angiò, D.; Fantini, A.; Fiorucci, M.; Iannucci, R.; Lenti, L.; Marmoni, G.M.; Martino, S. Environmental Forcings and Micro-Seismic Monitoring in a Rock Wall Prone to Fall during the 2018 Buran Winter Storm. *Nat. Hazards* **2021**, *106*, 2599–2617. [[CrossRef](#)]
18. Got, J.L.; Mourot, P.; Grangeon, J. Pre-Failure Behaviour of an Unstable Limestone Cliff from Displacement and Seismic Data. *Nat. Hazards Earth Syst. Sci.* **2010**, *10*, 819–829. [[CrossRef](#)]
19. Amitrano, D.; Arattano, M.; Chiarle, M.; Mortara, G.; Occhiena, C.; Pirulli, M.; Scavia, C. Microseismic Activity Analysis for the Study of the Rupture Mechanisms in Unstable Rock Masses. *Nat. Hazards Earth Syst. Sci.* **2010**, *10*, 831–841. [[CrossRef](#)]
20. Senfaute, G.; Duperret, A.; Lawrence, J.A. Micro-Seismic Precursory Cracks Prior to Rock-Fall on Coastal Chalk Cliffs: A Case Study at Mesnil-Val, Normandie, NW France. *Nat. Hazards Earth Syst. Sci.* **2009**, *9*, 1625–1641. [[CrossRef](#)]
21. Colombero, C. Microseismic Strategies for Characterization and Monitoring of an Unstable Rock Mass. Ph.D. Thesis, Università Degli Studi di Torino, Torino, Italy, 2017.
22. D’Angiò, D. Rheological Effects Related to Neo-Fracturing Processes in Rock Masses. Ph.D. Thesis, Sapienza University of Rome, Rome, Italy, 2019.
23. D’Angiò, D.; Lenti, L.; Martino, S. Microseismic Monitoring to Assess Rock Mass Damaging through a Novel Damping Ratio-Based Approach. *Int. J. Rock Mech. Min. Sci.* **2021**, *146*, 104883. [[CrossRef](#)]
24. Tang, C.; Li, L.; Xu, N.; Ma, K. Microseismic Monitoring and Numerical Simulation on the Stability of High-Steep Rock Slopes in Hydropower Engineering. *J. Rock Mech. Geotech. Eng.* **2015**, *7*, 493–508. [[CrossRef](#)]
25. Cai, M.; Kaiser, P.K.; Morioka, H.; Minami, M.; Maejima, T.; Tasaka, Y.; Kurose, H. FLAC/PFC Coupled Numerical Simulation of AE in Large-Scale Underground Excavations. *Int. J. Rock Mech. Min. Sci.* **2007**, *44*, 550–564. [[CrossRef](#)]
26. Xiao, Y.X.; Feng, X.T.; Hudson, J.A.; Chen, B.R.; Feng, G.L.; Liu, J.P. ISRM Suggested Method for In Situ Microseismic Monitoring of the Fracturing Process in Rock Masses. *Rock Mech. Rock Eng.* **2016**, *49*, 343–369. [[CrossRef](#)]
27. Vaezi, Y.; van der Baan, M. Analysis of Instrument Self-Noise and Microseismic Event Detection Using Power Spectral Density Estimates. *Geophys. J. Int.* **2014**, *197*, 1076–1089. [[CrossRef](#)]
28. Trnkoczy, A. Understanding and Parameter Setting of STA/LTA Trigger Algorithm. In *New Manual of Seismological Observatory Practice 2 (NMSOP-2)*; Bormann, P., Ed.; Deutsches GeoForschungsZentrum GFZ: Potsdam, Germany, 2012.
29. Provost, F.; Malet, J.P.; Hibert, C.; Helmstetter, A.; Radiguet, M.; Amitrano, D.; Langet, N.; Larose, E.; Abancó, C.; Hürlimann, M.; et al. Towards a Standard Typology of Endogenous Landslide Seismic Sources. *Earth Surf. Dyn.* **2018**, *6*, 1059–1088. [[CrossRef](#)]
30. Wenner, M.; Hibert, C.; Meier, L.; Walter, F. Near Real-Time Automated Classification of Seismic Signals of Slope Failures with Continuous Random Forests. *Nat. Hazards Earth Syst. Sci.* **2020**, *21*, 339–361. [[CrossRef](#)]
31. Peng, P.; He, Z.; Wang, L. Automatic Classification of Microseismic Signals Based on MFCC and GMM-HMM in Underground Mines. *Shock. Vib.* **2019**, *2019*, 5803184. [[CrossRef](#)]
32. Spillmann, T.; Maurer, H.; Green, A.G.; Heincke, B.; Willenberg, H.; Husen, S. Microseismic Investigation of an Unstable Mountain Slope in the Swiss Alps. *J. Geophys. Res. Solid Earth* **2007**, *112*, 1–25. [[CrossRef](#)]
33. Dai, F.; Li, B.; Xu, N.; Zhu, Y. Microseismic Early Warning of Surrounding Rock Mass Deformation in the Underground Powerhouse of the Houziyan Hydropower Station, China. *Tunn. Undergr. Space Technol.* **2017**, *62*, 64–74. [[CrossRef](#)]
34. Dai, F.; Li, B.; Xu, N.; Fan, Y.; Zhang, C. Deformation Forecasting and Stability Analysis of Large-Scale Underground Powerhouse Caverns from Microseismic Monitoring. *Int. J. Rock Mech. Min. Sci.* **2016**, *86*, 269–281. [[CrossRef](#)]
35. Liu, Q.S.; Wu, J.; Zhang, X.P.; Tang, L.X.; Bi, C.; Li, W.W.; Xu, J.L. Microseismic Monitoring to Characterize Structure-Type Rockbursts: A Case Study of a TBM-Excavated Tunnel. *Rock Mech. Rock Eng.* **2020**, *53*, 2995–3013. [[CrossRef](#)]
36. Xu, N.W.; Li, T.B.; Dai, F.; Zhang, R.; Tang, C.A.; Tang, L.X. Microseismic Monitoring of Strainburst Activities in Deep Tunnels at the Jinping II Hydropower Station, China. *Rock Mech. Rock Eng.* **2016**, *49*, 981–1000. [[CrossRef](#)]
37. Carlà, T.; Farina, P.; Intrieri, E.; Botsialas, K.; Casagli, N. On the Monitoring and Early-Warning of Brittle Slope Failures in Hard Rock Masses: Examples from an Open-Pit Mine. *Eng. Geol.* **2017**, *228*, 71–81. [[CrossRef](#)]
38. Hudyma, M.; Potvin, Y.H. An Engineering Approach to Seismic Risk Management in Hardrock Mines. *Rock Mech. Rock Eng.* **2010**, *43*, 891–906. [[CrossRef](#)]
39. Wesseloo, J.; Sweby, G. *Microseismic Monitoring of Hard Rock Mine Slopes*; Australian Centre for Geomechanics: Perth, Australia, 2008; pp. 433–450. [[CrossRef](#)]
40. Ma, J.; Guan, J.; Duan, J.; Huang, L.; Liang, Y. Stability Analysis on Tunnels with Karst Caves Using the Distinct Lattice Spring Model. *Undergr. Space* **2021**, *6*, 469–481. [[CrossRef](#)]
41. Iannucci, R.; Lenti, L.; Martino, S. Seismic Monitoring System for Landslide Hazard Assessment and Risk Management at the Drainage Plant of the Peschiera Springs (Central Italy). *Eng. Geol.* **2020**, *277*, 105787. [[CrossRef](#)]
42. Amitrano, D.; Gaffet, S.; Malet, J.-P.; Maquaire, O. Understanding Mudslides through Micro-Seismic Monitoring: The Super-Sauze (South-East French Alps) Case Study. *Bull. Société Géologique Fr.* **2007**, *178*, 149–157. [[CrossRef](#)]

43. Helmstetter, A.; Garambois, S. Seismic Monitoring of Schilienne Rockslide (French Alps): Analysis of Seismic Signals and Their Correlation with Rainfalls. *J. Geophys. Res. Earth Surf.* **2010**, *115*, 1–15. [[CrossRef](#)]
44. Occhiena, C.; Pirulli, M. Analysis of Climatic Influences on Slope Microseismic Activity and Rockfalls: Case Study of the Matterhorn Peak (Northwestern Alps). *J. Geotech. Geoenviron. Eng.* **2012**, *138*, 1012–1021. [[CrossRef](#)]
45. Fiorucci, M.; Martino, S.; Bozzano, F.; Prestininzi, A. Comparison of Approaches for Data Analysis of Multi-Parametric Monitoring Systems: Insights from the Acuto Test-Site (Central Italy). *Appl. Sci.* **2020**, *10*, 7658. [[CrossRef](#)]
46. Accordi, G.; Carbone, F.; Civitelli, G.; Corda, L.; de Rita, D.; Esu, D.; Funicello, R.; Kotsakis, T.; Mariotti, G.; Sposato, A. Lithofacies Map of Latium-Abruzzi and Neighbouring Areas. *Quad. Ric. Sci.* **1986**, *114*, 223.
47. Grechi, G.; Angiò, D.D.; Fiorucci, M.; Iannucci, R.; Lenti, L.; Marco, G.; Martino, S. Integrated Geophysical and Geotechnical Monitoring for Multiscale Rock Mass Damaging Investigation at the Acuto Field-Lab (Italy). In Proceedings of the 23rd EGU General Assembly, Online, 19–30 April 2021.
48. Fiorucci, M.; Marmoni, G.M.; Martino, S.; Mazzanti, P. Thermal Response of Jointed Rock Masses Inferred from Infrared Thermographic Surveying (Acuto Test-Site, Italy). *Sensors* **2018**, *18*, 2221. [[CrossRef](#)] [[PubMed](#)]
49. Grechi, G.; Fiorucci, M.; Marmoni, G.M.; Martino, S. 3D Thermal Monitoring of Jointed Rock Masses through Infrared Thermography and Photogrammetry. *Remote Sens.* **2021**, *13*, 957. [[CrossRef](#)]
50. Marmoni, G.M.; Fiorucci, M.; Grechi, G.; Martino, S. Modelling of Thermo-Mechanical Effects in a Rock Quarry Wall Induced by near-Surface Temperature Fluctuations. *Int. J. Rock Mech. Min. Sci.* **2020**, *134*, 104440. [[CrossRef](#)]
51. Li, X.; Shang, X.; Wang, Z.; Dong, L.; Weng, L. Identifying P-Phase Arrivals with Noise: An Improved Kurtosis Method Based on DWT and STA/LTA. *J. Appl. Geophys.* **2016**, *133*, 50–61. [[CrossRef](#)]
52. Withers, M.; Aster, R.; Young, C.; Beiriger, J.; Harris, M.; Moore, S.; Trujillo, J. A Comparison of Select Trigger Algorithms for Automated Global Seismic Phase and Event Detection. *Bull. Seismol. Soc. Am.* **1998**, *88*, 95–106. [[CrossRef](#)]
53. Benitez, M.C.; Ramirez, J.; Segura, J.C.; Ibanez, J.M.; Almendros, J.; Garcia-Yeguas, A.; Cortes, G. Continuous HMM-Based Seismic-Event Classification at Deception Island, Antarctica. *IEEE Trans. Geosci. Remote Sens.* **2007**, *45*, 138–146. [[CrossRef](#)]
54. Qu, S.; Guan, Z.; Verschuur, E.; Chen, Y. Automatic High-Resolution Microseismic Event Detection via Supervised Machine Learning. *Geophys. J. Int.* **2020**, *222*, 1881–1895. [[CrossRef](#)]
55. Hibert, C.; Mangeney, A.; Grandjean, G.; Baillard, C.; Rivet, D.; Shapiro, N.M.; Satriano, C.; Maggi, A.; Boissier, P.; Ferrazzini, V.; et al. Automated Identification, Location, and Volume Estimation of Rockfalls at Piton de La Fournaise Volcano. *J. Geophys. Res. Earth Surf.* **2014**, *119*, 1082–1105. [[CrossRef](#)]
56. Hibert, C.; Provost, F.; Malet, J.P.; Maggi, A.; Stumpf, A.; Ferrazzini, V. Automatic Identification of Rockfalls and Volcano-Tectonic Earthquakes at the Piton de La Fournaise Volcano Using a Random Forest Algorithm. *J. Volcanol. Geotherm. Res.* **2017**, *340*, 130–142. [[CrossRef](#)]
57. Meyer, M.; Weber, S.; Beutel, J.; Thiele, L. Systematic Identification of External Influences in Multi-Year Microseismic Recordings Using Convolutional Neural Networks. *Earth Surf. Dyn.* **2019**, *7*, 171–190. [[CrossRef](#)]
58. Bommer, J.J.; Stafford, P.J.; Alarcón, J.E. Empirical Equations for the Prediction of the Significant, Bracketed, and Uniform Duration of Earthquake Ground Motion. *Bull. Seismol. Soc. Am.* **2009**, *99*, 3217–3233. [[CrossRef](#)]
59. Gutenberg, B.; Richter, C.F. *Seismicity of the Earth and Associated Phenomena*, 2nd ed.; Princeton University Press: Princeton, NJ, USA, 1954.
60. Wilson, R.C. *Relation of Arias Intensity to Magnitude and Distance in California*; US Geological Survey: Menlo Park, CA, USA, 1993.
61. Zhan, Z. Gutenberg–Richter Law for Deep Earthquakes Revisited: A Dual-Mechanism Hypothesis. *Earth Planet Sci. Lett.* **2017**, *461*, 1–7. [[CrossRef](#)]
62. Occhiena, C.; Coviello, V.; Arattano, M.; Chiarle, M.; Morra Di Cella, U.; Pirulli, M.; Pogliotti, P.; Scavia, C. Analysis of Microseismic Signals and Temperature Recordings for Rock Slope Stability Investigations in High Mountain Areas. *Nat. Hazards Earth Syst. Sci.* **2012**, *12*, 2283–2298. [[CrossRef](#)]
63. Frayssines, M.; Hantz, D. Failure Mechanisms and Triggering Factors in Calcareous Cliffs of the Subalpine Ranges (French Alps). *Eng. Geol.* **2006**, *86*, 256–270. [[CrossRef](#)]

Disclaimer/Publisher’s Note: The statements, opinions and data contained in all publications are solely those of the individual author(s) and contributor(s) and not of MDPI and/or the editor(s). MDPI and/or the editor(s) disclaim responsibility for any injury to people or property resulting from any ideas, methods, instructions or products referred to in the content.